Lithos 370–371 (2020) 105644

Contents lists available at ScienceDirect

Lithos

journal homepage: www.elsevier.com/locate/lithos

Research Article

Amphibole and whole-rock geochemistry of early Late Jurassic diorites, Central Tibet: Implications for petrogenesis and geodynamic processes

Wan-Long Hu [a,b], Qiang Wang [a,b,c,*], Jin-Hui Yang [d], Gong-Jian Tang [a,c], Yue Qi [a], Lin Ma [a], Zong-Yong Yang [a], Peng Sun [a]

[a] State Key Laboratory of Isotope Geochemistry, Guangzhou Institute of Geochemistry, Chinese Academy of Sciences, Guangzhou 510640, China
[b] College of Earth and Planetary Sciences, University of Chinese Academy of Sciences, Beijing 100049, China
[c] CAS Center for Excellence in Tibetan Plateau Earth Sciences, Beijing 100101, China
[d] Institute of Geology and Geophysics, Chinese Academy of Sciences, Beijing 100029, China

ARTICLE INFO

Article history:
Received 14 September 2019
Accepted 14 June 2020
Available online 19 June 2020

Keywords:
Amphibole
Diorite
Arc magma
Thermobarometry
Central Tibet

ABSTRACT

Arc magmas are generated by complex geological processes in subduction settings. Due to the complexity of source materials and geological processes, the genesis of arc magmatic rocks can be difficult to disentangle. Here, we report on diorites from the Kenama area of the middle-eastern part of the Bangong–Nujiang suture zone in central Tibet. New SIMS and LA–ICP–MS zircon U—Pb dating for three diorite samples indicates that they crystallized during the early Late Jurassic (ca. 161 Ma). The diorites can be divided into two groups based on whole-rock major element compositions and mineralogical characteristics: Group I diorites with relatively low SiO_2 (47.6–53.4 wt%), and high MgO (4.97–9.10 wt%) and amphibole contents (50–54 vol%); and Group II diorites with slightly higher SiO_2 (56.9–59.5 wt%), and low MgO (2.9–3.8 wt%) and amphibole contents (25–30 vol%). The Group I diorites exhibit relative enrichment in light rare earth element (LREE) ($(La/Yb)_N$ = 5.7–10.5) with slightly negative Eu anomalies, and are characterized by enrichment of large ion lithophile elements (LILEs; K, Rb, Ba, Th, and U), the depletion of high field strength elements (HFSEs; Nb, Ta, Zr, Hf, and Ti). The Group I diorites have relatively high initial $^{87}Sr/^{86}Sr$ ratios (0.7073–0.7094), variably negative $\varepsilon_{Nd}(t)$ values (−10.3 to −5.9), negative zircon $\varepsilon_{Hf}(t)$ values (−14.8 to–4.4), and slightly elevated $\delta^{18}O$ values (6.5‰–7.3‰). The Group II diorites show similar trace element characteristics to Group I. They also have high initial $^{87}Sr/^{86}Sr$ ratios (0.7083–0.7087), uniformly negative $\varepsilon_{Nd}(t)$ values (−9.5 to −9.0), negative zircon $\varepsilon_{Hf}(t)$ values (−10.3 to −4.2), and elevated $\delta^{18}O$ values (6.6‰–7.5‰). Amphiboles from Group I and Group II diorites have low Al_2O_3 contents (3.6–9.9 wt% and 5.6–8.5 wt%, respectively), and formed at similar P–T conditions (751–871 °C and 69–226 MPa and 745–832 °C and 77–162 MPa, respectively). On primitive mantle-normalized spider diagrams, these low-Al amphibole grains have slightly convex upward REE patterns with distinctly negative anomalies in Pb, Sr, Eu, Zr, Hf, and Ti, suggesting that amphiboles from both groups crystallized from the similar arc magmas after plagioclase and magnetite crystallization. These mineralogical, geochemical and isotopic characteristics suggest that both groups of Kenama diorites probably originated from an enriched lithospheric mantle metasomatized by subducted oceanic sediment-derived melts. Their parental magmas may have similar geochemical characteristics and underwent varying degrees of accumulation and fractional crystallization. The Group I diorites were likely generated by accumulation of amphibole and fractional crystallization of olivine, clinopyroxene, and plagioclase from mafic magmas, and the Group II diorites were formed by the fractional crystallization of clinopyroxene and plagioclase from mafic magmas that were geochemically similar to the Group I diorites. In combination with regional geology, in particular adjacent ophiolites, high-magnesian andesitic rocks and Cretaceous sedimentary rocks, we conclude that all of the Kenama diorites were probably generated in an early Late Jurassic arc setting related to the subduction of the Bangong–Nujiang Tethys oceanic lithosphere.

1. Introduction

Arc magmas in subduction settings encompass components derived from various reservoirs (e.g., Kelemen et al., 2014), including the slab and sub-arc mantle, continental materials from subduction erosion, and the overlying crust (e.g., Jones et al., 2015; Schmidt and Poli,

* Corresponding author at: State Key Laboratory of Isotope Geochemistry (SKLaBIG), Guangzhou Institute of Geochemistry (GIG), Chinese Academy of Sciences (CAS), Wushan Street, Guangzhou 510640, China.
E-mail address: wqiang@gig.ac.cn (Q. Wang).

https://doi.org/10.1016/j.lithos.2020.105644
0024-4937/

2014). Hence, arc magmas are the outcome of various factors and processes (Davidson et al., 2005), including the degree and regime of source melting (equilibrium/disequilibrium), fractional crystallization (possibly accompanied by assimilation), and hybridization between different magmas, ranging from magmas from the deep crust to those at the depth of emplacement (Brown, 2013; Shellnutt and Zellmer, 2010). Due to the complexity of source materials and geological processes, the genesis of arc magmatic rocks can be difficult to disentangle (Rocchi et al., 2015).

The Tibetan Plateau, from north to south, consists of four main continental terranes: the Songpan–Ganze, Qiangtang, Lhasa, and Himalaya, which are separated by the Jinsha suture zone (JSSZ), Bangong–Nujiang suture zone (BNSZ), and Indus–Yarlung Zangbo suture zone (IYZSZ), respectively (Fig. 1a; Pan et al., 2012; Yin and Harrison, 2000). In central Tibet, the BNSZ was formed by the collision of the Qiangtang and Lhasa terranes (Fig. 1b). Magmatic rocks are well distributed along the BNSZ, which is characterized by two Jurassic–Cretaceous magmatic arcs, one in the southern Qiangtang subterrane to the north and the other in the northern Lhasa subterrane to the south (e.g., Liu et al., 2017; Zhu et al., 2016 and references therein). Magmatic arc activity along the northern Lhasa subterranes was probably related to subduction of the Bangong–Nujiang Tethys Oceanic lithosphere (Fig. 1b) (e.g., Sui et al., 2013; Zeng et al., 2016; Zhu et al., 2013, 2016). This magmatic belt records important information on the Late Mesozoic crustal architecture and tectonomagmatic evolution of the northern Lhasa subterrane. The rocks of this magmatic belt are best exposed in the northern Lhasa subterrane, which includes the Along Tso Batholith and Yanhu volcanic rocks in the west, and the Nyima volcanic rocks, and Baingoin Batholith, and Daru Tso volcanic rocks in the east (Fig. 1b). Most of these arc magmatic rocks mainly formed during the Jurassic–Cretaceous and consist of intermediate–felsic rocks. The Jurassic–Cretaceous magmatic rocks provide a window for examining the evolution of the Bangong–Nujiang Tethys Ocean (BNTO).

In this study, we report new zircon U—Pb ages and Hf—O isotopes, amphibole compositions, whole-rock geochemistry, and Sr—Nd isotopic compositions for diorites from the Kenama area in the BNSZ. Based on field observations and petrography, coupled with our new data, we constrain its petrogenesis and source characteristics, and shed new light on the formation processes of arc magmas and evolution of the BNTO.

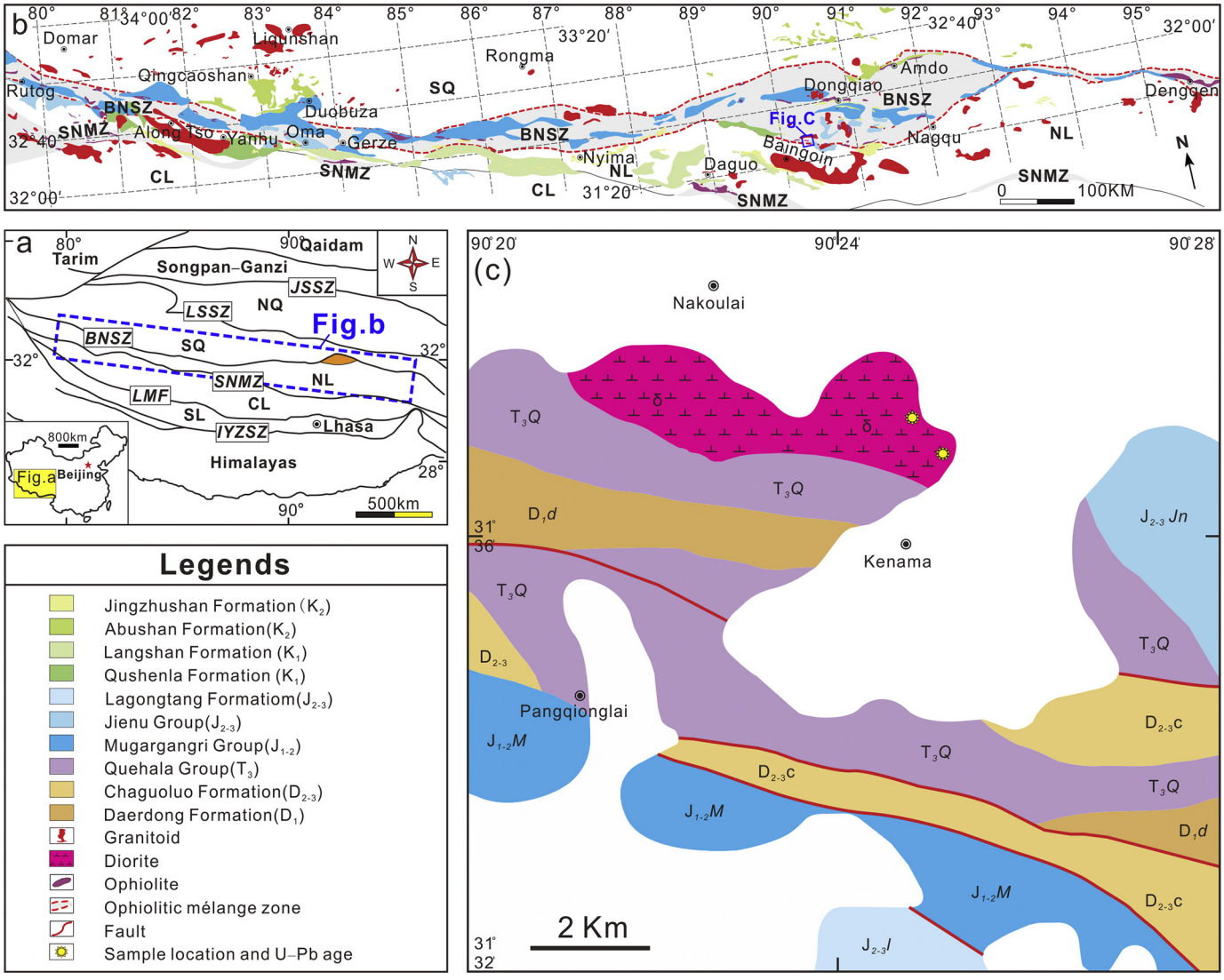

Fig. 1. (a) Sketch geological map of Tibet. JSSZ = Jinsha suture zone; NQ = Northern Qiangtang subterrane; LSSZ = Longmu Co–Shuanghu suture zone; SQ = Southern Qiangtang subterrane; BNSZ = Bangong–Nujiang suture zone; NL = Northern Lhasa subterrane; SNMZ = Shiquan River–Nam Tso Mélange zone; CL = Central Lhasa subterrane; LMF = Luobadui–Milashan Fault; SL = Southern Lhasa subterrane; IYZSZ = Indus–Yarlung Zangbo suture zone. (b) Geological map of the Bangong–Nujiang suture zone (modified after Zhu et al., 2016). (c) Geological map of the Kenama area.

2. Geological setting and petrography

The BNSZ in central Tibet extends east–west for more than 2000 km through the Bangong Co, Gerze, Dongqiao, Dengqen, and Jiayuqiao regions, and into Burma, Thailand, and Malaysia. It marks the boundary between the Qiangtang terrane to the north and the Lhasa terrane to the south (Fig. 1a; Yin and Harrison, 2000; Zhu et al., 2016). The suture zone consists of scattered ophiolitic fragments, radiolarian cherts, oceanic island (or seamount), arc volcanic-magmatic rocks, flysch-like deposits, and accretionary complexes (Fig. 1b; e.g., Fan et al., 2015b; Li et al., 2018, 2019; Liu et al., 2016; Ma et al., 2017; Wang et al., 2016; Zhu et al., 2016), and provides an important record of continental breakup and drift, and accretion-related tectonism, magmatism, sedimentation, and metamorphism (e.g., Liu et al., 2016; Wang et al., 2016; Zhang et al., 2014; Zhu et al., 2016 and references therein). Jurassic–Cretaceous ophiolitic mélanges are distributed irregularly along the BNSZ (Wang et al., 2016). The ages of Amdo gneiss and high-pressure granulite-facies metamorphism indicate metamorphism within the BNSZ occurred in the Early–Middle Jurassic (Zhang et al., 2014; Zhu et al., 2016). The Amdo terrane is an isolated microcontinent within the BNSZ and has ancient crystalline basement (Guynn et al., 2006, 2012; Zhu et al., 2011), whereas the northern Lhasa subterrane mainly consists of juvenile crust (Zhu et al., 2011). The Jurassic to Lower Cretaceous sedimentation units are widely distributed along/across the BNSZ and unconformably overlain by the Upper Cretaceous terrestrial molasse of the Jingzhushan and Abushan Formations, respectively (Fig. 1b; Wang et al., 2013; Zhu et al., 2016 and references therein). Magmatic rocks are also widespread along the BNSZ (Fig. 1b), including two Jurassic–Cretaceous magmatic arcs: the Caima–Duobuza–Rongma–Kangqiong–North Amdo magmatic belt and the Along Tso–Yanhu–Daguo–Baingoin–Daru Tso magmatic belt (Zhu et al., 2016 and references therein).

Despite decades of studies, the subduction process and the closure time of the BNTO remains unresolved. The subduction of the Bangong–Nujiang oceanic lithosphere was possibly initiated no later than the early Late Jurassic based on the presence of the ~164 Ma high-magnesium andesitic rocks identified from the Daru Tso and Jiaqiong areas (Tang et al., 2019; Zeng et al., 2016). However, Ma et al. (2017) proposed that the Lhasa–Qiangtang collision took place in late Middle Jurassic time (ca. 166 Ma), based on the field observation of an angular unconformity that truncated the Jurassic succession and the recognition of siliciclastic provenance changed from arc magmatic sources to uplifted orogenic sources in the vicinity of the Jiaqiong area (Biluoco–Qixiangco area). Through comparison of numerous studies on rocks (ophiolites, sedimentary rocks, boninitic dikes, Jurassic-Cretaceous magmatic rocks, and ocean island basalts (OIBs)) and paleomagnetic data, we find that the subduction termination and the oceanic basin closure time ranged from mid-Jurassic (~166 Ma) to late Early Cretaceous (~108 Ma) (e.g., Cao et al., 2019, 2020; Fan et al., 2015a, 2015b, 2017; Hao et al., 2016, 2019; Lai et al., 2019; Li et al., 2014; Ma et al., 2017; Wang et al., 2016; Xu et al., 2015; Zhong et al., 2017; Zhu et al., 2016; Zhu et al., 2018; Zhu et al., 2019b). Hence, the closure time of the BNTO remains highly debate.

The Kenama diorites are stocks that have intruded into the upper Triassic Quehala Group and have an outcrop area of ~9.0 km^2 (Fig. 1c). These diorites are distributed in the southern margin of the suture zone and belong to the Along Tso–Yanhu–Daguo–Baingoin–Daru Tso magmatic belt (Fig. 1b). The upper Triassic Quehala Group consists mainly of conglomerate and sandstone. Diorite samples investigated in this study were collected ~45 km northeast of the Baingoin county within the middle-eastern segment of the BNSZ, at 90°25′16.7″E, 31°36′58.1″N (Fig. 1c). Based on mineralogical characteristics (Fig. 2), the diorites can be divided into two groups: the Group I diorites (Fig. 2c) contain much more amphibole than those in Group II (Fig. 2d). Group I diorites are dark green, medium- to coarse-grained (Fig. 2a), and contain plagioclase (40–45 vol%), amphibole (50–54 vol%), and minor quartz (0–1 vol%). Chlorite, epidote, and sericite are secondary minerals. Fe—Ti oxides, zircon, and titanite are common accessory minerals. Plagioclase occurs as discrete euhedral phenocrysts that are locally altered to be sericite and kaolinite. Some plagioclase phenocrysts have been altered to zoisite, epidote and albite. Amphiboles grains are subhedral, vary in color from dark puce and dark blue to opaque, and contain abundant inclusions of plagioclase, apatite, epidote, and Fe—Ti oxides (Fig. 2c, e). Group II diorites are medium-grained, grayish white to grayish in color (Fig. 2b), and contain plagioclase (60–65 vol%), amphibole (25–30 vol%), and minor quartz (3–5 vol%). Epidote and chlorite are secondary minerals and accessory minerals include zircon, apatite, titanite, and Fe—Ti oxides. Plagioclase is variably affected by sericitization and epidotization. Amphiboles are present as subhedral–euhedral crystals that are commonly twinned and partly altered to chlorite. They are poikilitic, with inclusions of plagioclase, apatite, and Fe—Ti oxides (Fig. 2d, f).

3. Analytical methods

3.1. Zircon U—Pb dating and Hf—O isotopic analyses

Zircons were separated by using conventional heavy liquid and magnetic separation techniques. Representative zircon grains were handpicked and mounted in an epoxy resin disc, and then polished to expose the grain centers. Cathodoluminescence (CL) images were obtained for zircons prior to analysis, using a JEOL JXA-8100 Superprobe at the State Key Laboratory of Isotope Geochemistry, Guangzhou Institute of Geochemistry, Chinese Academy of Sciences (SKLaBIG GIG CAS), in order to characterize internal structures and choose potential target sites for U—Pb dating and Hf—O isotopic analyses.

Laser ablation (LA)–ICP–MS zircon U—Pb analyses were performed at the Institute of Geology and Geophysics, Chinese Academy of Sciences (IGG CAS) in Beijing. Laser ablation was accomplished using a Geolas-193 laser-ablation system equipped with a 193 nm ArFexcimer laser and connected to an ELAN6100 DRC ICP–MS. The analyses were conducted with a spot diameter of 35 μm with a typical ablation time of approximately 30 s for 200 cycles of each measurement, an 8 Hz repetition rate, and a laser power of 100 mJ/pulse. A more detailed description of the analytical technique is provided by Xie et al. (2008). The isotopic ratios and element concentrations of zircon were calculated with GLITTER 4.4. LA–ICP–MS zircon U—Pb isotopic data are presented in Table S1.

Secondary ion mass spectrometry (SIMS) zircon U—Pb analyses were conducted using a CAMECA IMS-1280-HR system at the SKLaBIG GIG CAS. Analytical procedures are similar to that described by Li et al. (2009). The analytical ellipsoidal spot is about 20 μm × 30 μm in size. The standard zircon Plešovice (Sláma et al., 2008) were used to correct U–Th–Pb ratios and their absolute abundances. Measured compositions were corrected for common Pb using non-radiogenic ^{204}Pb. The secondary standard zircon Qinghu were analyzed as unknown samples to monitor the reliability of the whole procedure. During the course of this study, five Qinghu zircon spots were analyzed and yielded a mean age of 158.8 ± 0.3 Ma, which is within error of the recommended value of 159.5 ± 0.2 Ma (Li et al., 2013). Concordia plots and weighted mean U—Pb ages with 1σ were processed using the Isoplot/Ex v.3.0 program (Ludwig, 2003). SIMS zircon U—Pb isotopic data are presented in Table S2.

Subsequently, zircon oxygen isotopes were also measured using the SIMS at the SKLaBIG GIG CAS. The detailed analytical procedures were similar to those described by Li et al. (2010a). The size of analytical spots is about 20 μm in diameter. The measured oxygen isotopic data were corrected for instrumental mass fractionation (IMF) using the Penglai zircon standard ($\delta^{18}O_{VSMOW}$ = 5.3‰, Li et al., 2010b). The internal precision of a single analysis generally was better than 0.12‰ (SE) for the $^{18}O/^{16}O$ ratio. The external precision, measured by the reproducibility of repeated analyses of Penglai standard, is 0.16‰ (SD, n = 18). Nine measurements of the Qinghu

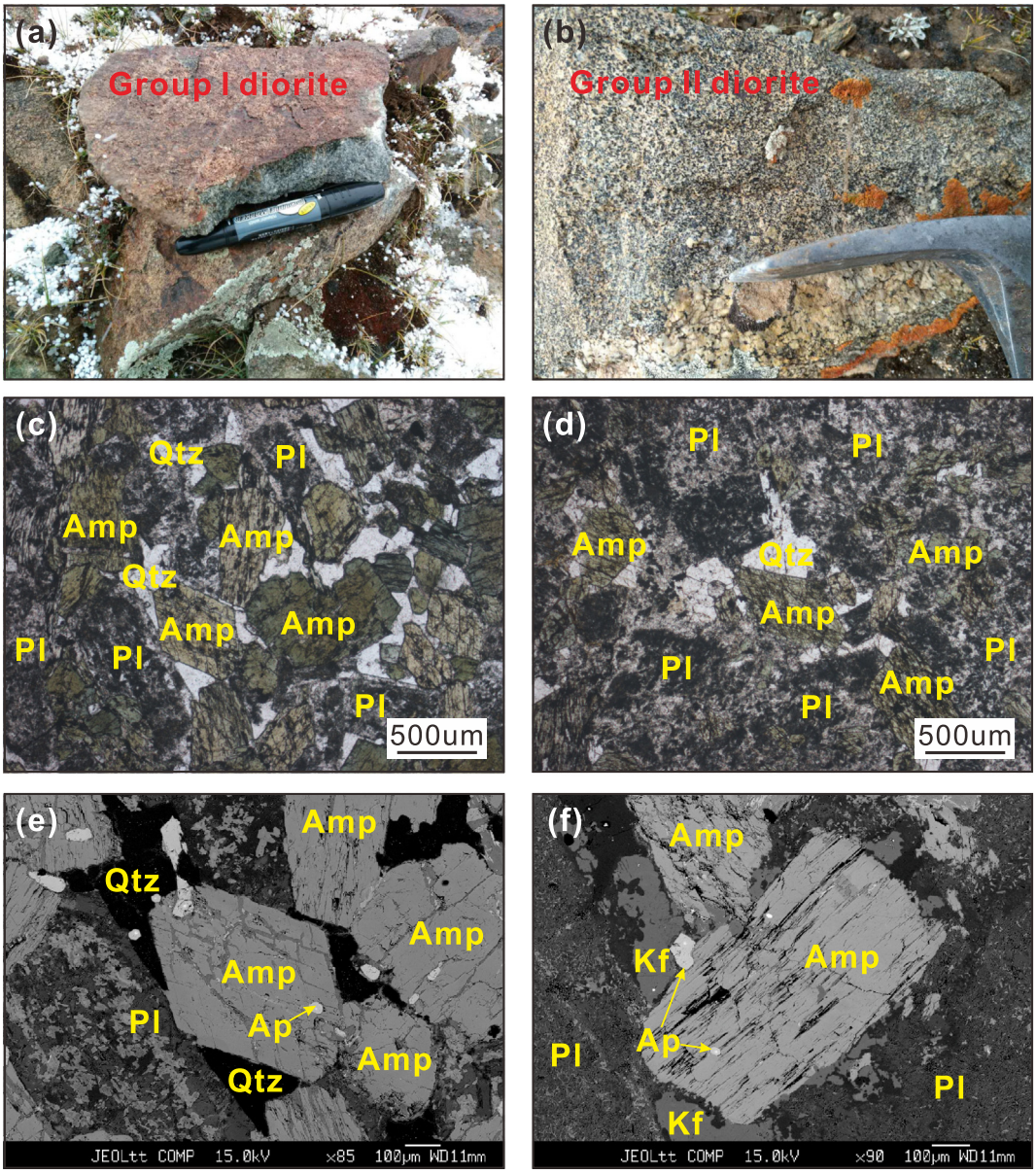

Fig. 2. Representative field photographs, photomicrographs (plane-polarized light) and backscattered electron (BSE) images illustrating the petrographic characteristics of the Kenama Group I (a, c, and e) and the Group II diorites (b, d, and f). Mineral abbreviations: Amp: amphibole; Pl: plagioclase; Qtz: quartz; Kf: K–feldspar; Ap: apatite.

zircon standard during the course of this study yielded a weighted mean of $\delta^{18}O = 5.49 \pm 0.11‰$ (SD), which is consistent within errors with the reported value of 5.4 ± 0.2‰ (Li et al., 2013). Zircon oxygen isotopic data are listed in Table S7.

In situ zircon Lu—Hf isotopic analyses were carried out on a Neptune Plus multi-collector ICP-MS equipped with a RESOlution M-50193 nm laser-ablation system at the SKLaBIG GIG CAS. Lu—Hf isotopic analyses were conducted on the same zircon grains that were previously analyzed for U—Pb and/or O isotopes, with ablation pits of 45 μm in diameter, ablation time of 30s, repetition rate of 6 Hz, and laser beam energy density of 4 J/cm^2. The detailed analytical procedures are similar to those described by Zhang et al. (2015). Measured $^{176}Hf/^{177}Hf$ ratios were normalized to $^{179}Hf/^{177}Hf = 0.7325$. Thirteen measurements of the Penglai zircon standard during the course of this study yielded a weighted mean of $^{176}Hf/^{177}Hf = 0.282906 \pm 0.000021$ (SD), which is consistent within errors with the reported value in Li et al. (2010b). Zircon Hf isotopic data are listed in Table S7.

3.2. Mineral chemistry analyses

All silicate mineral analyses and back–scattered–electron (BSE) imaging were carried out at the SKLaBIG GIG CAS using a JXA–8100 electron microprobe. An accelerating voltage of 15 kV, a specimen current of 20 nA, and a beam size of 1–2 μm were employed. The analytical errors are generally less than 2%. The analytical procedures were described in detail in Huang et al. (2007). The results are presented in Table S3.

In situ trace element compositions of minerals were measured with an ELEMENT XR (Thermo Fisher Scientific) ICP–MS coupled with a 193-nm (ArF) Resonetics RESOlution M-50 laser ablation system at the SKLaBIG GIG CAS. Laser spots on sample material were ~ 33 μm in diameter. The calibration line for each element was constructed by analyzing three USGS reference glasses (BCR–2G, BHVO–2G and GSD–1G) with Si as an internal standard element. The secondary reference glasses TB–1G were analyzed as unknown samples to monitor the reliability of the whole procedure. 25 analyses of TB–1G indicate most elements are

within 8% of the reference values and the analytical precision (2RSD) was better than 10% for most elements (Table S8). Detailed experiment procedures and data reduction strategy were described in Zhang et al. (2019). The results are presented in Table S4.

3.3. Whole-rock element and Sr—Nd isotopic analyses

Rock samples were examined by optical microscopy and unaltered or least-altered samples were selected for geochemical analyses. The rocks were sawed into small chips, ultrasonically cleaned in distilled water with <3% HNO_3 and then in deionized water alone, and subsequently dried and handpicked to remove visible contamination. The rocks were crushed by a jaw crusher and then powdered to ~200 mesh in an agate mill, and the powder was used for analyses of major and trace elements, and Sr—Nd isotopes, at the SKLaBIG GIG CAS.

Major element oxides were analyzed on fused glass beads using a Rigaku RIX 2000 X-ray fluorescence spectrometer. The analytical procedures were the same as those described by Li et al. (2000). Glass discs were made by melting dehydrated sample powders. Calibration lines used in quantification were produced by bivariate regression of data from 36 reference materials encompassing a wide range of silicate compositions (Li et al., 2005), and analytical uncertainties are between 1% and 5%. Trace elements were analyzed by inductively coupled plasma mass spectrometry (ICP–MS), using a Perkin-Elmer Sciex ELAN 6000 instrument. Analytical procedures are the same as those described by Li et al. (2002). An internal standard solution containing the single element Rh was used to monitor signal drift during counting. A set of USGS and Chinese national rock standards, including BHVO–2, AGV–2, W–2a, GSR–1, and GSR–2 were chosen for calibration. Repeated runs give <3% RSD (relative standard deviation) for most elements of reference materials for ICP-MS analysis. Geochemical results are listed in Table S5.

The Sr—Nd isotopic compositions of selected samples were determined using a Neptune multicollector–ICP–MS (MC–ICP–MS). Analytical procedures are similar to those described in Li et al. (2004). Sr and REE were separated using cation columns, and Nd fractions were further separated by HDEHP-coated Kef columns. The $^{87}Sr/^{86}Sr$ ratio of the NBS987 standard and $^{143}Nd/^{144}Nd$ ratio of the Shin Etsu JNdi–1 standard were 0.710257 ± 0.000018 (n = 15, 2SD) and 0.512100 ± 0.000010 (n = 15, 2SD), respectively. All measured $^{143}Nd/^{144}Nd$ and $^{86}Sr/^{88}Sr$ ratios were normalized to $^{146}Nd/^{144}Nd$ = 0.7219 and $^{86}Sr/^{88}Sr$ = 0.1194, respectively. The Sr—Nd isotope results are listed in Table S6. The Sr—Nd isotopes of USGS reference material BHVO–2 of this study gave $^{87}Sr/^{86}Sr$ = 0.703480 ± 0.000007 (SE), $^{143}Nd/^{144}Nd$ = 0.512983 ± 0.000007 (SE), respectively, within the analytical error of the recommended values.

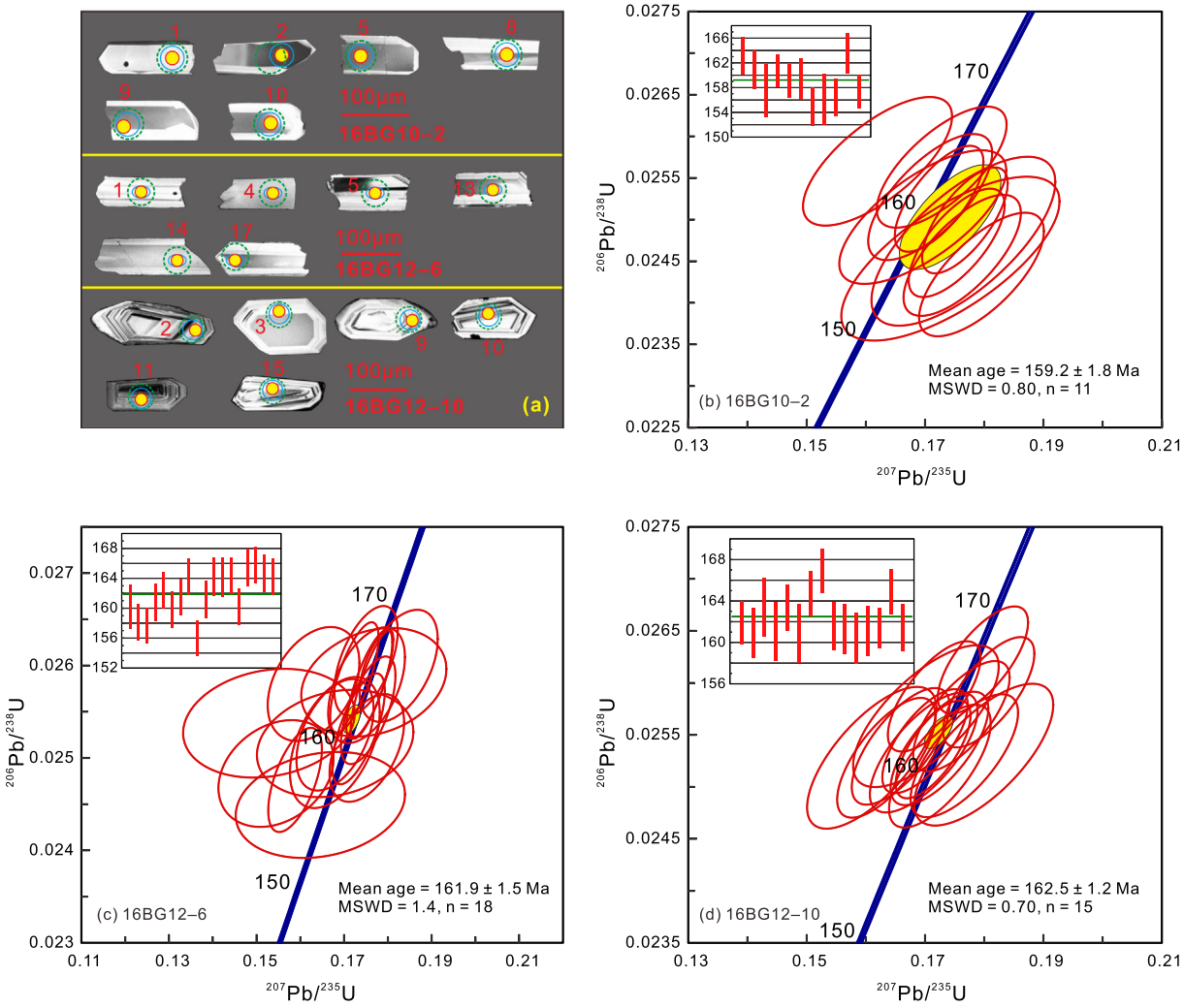

Fig. 3. (a) Representative CL images and (b–d) U—Pb concordia diagrams for zircons from the Kenama diorites. Blue solid circles and ellipses show the LA–MC–ICP–MS and SIMS spots analyzed for U—Pb dating, respectively; yellow circles with a red outline denote the spots analyzed for O isotopes; green dashed circles mark the spots analyzed for Hf isotopes.

4. Results

4.1. Zircon U—Pb ages

Group I diorite samples (16BG10–2 and 16BG12–6) were selected for zircon dating. Zircons in these samples have crystal lengths of ~100–200 μm and length-to-width ratios from 1:1 to 2:1. The crystals commonly show banded structures under cathodoluminescence (CL) (Fig. 3a), indicating crystallization from a mafic magma (Hoskin and Schaltegger, 2003). The analyzed zircon grains in samples 16BG10–2 and 16BG12–6 show variable contents of U (246–955 and 141–1492 ppm, respectively) and Th (358–2166 and 145–2942 ppm, respectively) and high Th/U ratios (1.22 to 2.27 and 0.74 to 3.70, respectively). Eleven spot analyses of zircons from sample 16BG10–2 yield concordant $^{206}Pb/^{238}U$ ages ranging from 155.0 to 163.6 Ma (LA–ICP–MS), with a weighted-mean $^{206}Pb/^{238}U$ age of 159.2 ± 1.8 Ma (MSWD = 0.8; Fig. 3b). Eighteen zircon grains from sample 16BG12–6 show a uniformly distributed concordant $^{206}Pb/^{238}U$ age of 156.0 to 165.8 Ma (SIMS), with a weighted-mean $^{206}Pb/^{238}U$ age of 161.9 ± 1.5 Ma (MSWD = 1.4; Fig. 3c).

Zircons extracted from a Group II diorite sample 16BG12–10 show oscillatory zoning in CL images and have crystal lengths of ~100–200 μm and length/width ratios of 2:1 to 3:1 (Fig. 3a), indicating a magmatic origin (Hoskin and Schaltegger, 2003). The analyzed zircon grains have variable contents of U (138–414 ppm) and Th (125–418 ppm), and Th/U ratios ranging from 0.73 to 1.22, also confirming a magmatic origin. Fifteen spot analyses of zircons yield concordant $^{206}Pb/^{238}U$ ages of 160.4 to 166.9 Ma (LA–ICP–MS), with a weighted-mean $^{206}Pb/^{238}U$ age of 162.5 ± 1.2 Ma (MSWD = 0.7; Fig. 3d).

4.2. Mineral compositions

According to the classification of amphibole, the Kenama diorites only contain Mg-hornblende (Si > 6.5; Fig. 4a; Leake et al., 1997; Hawthorne and Oberti, 2007). In this study, amphibole grains can be classified into a low-Al area (Al_2O_3 < 10 wt%, Si/Al_{tot} > 4; Fig. 4b). Based on the major element compositions of amphiboles, low-Al amphiboles in Group II diorites have lower MgO contents (Figure S1d) and higher FeO, K_2O, and Cl contents than the amphiboles in Group I diorites (Figure S1c, S1g–h). The amphibole $Mg^{\#}$ ($Mg/(Mg + Fe^{2+})$) values for the Group I diorites range from 0.64 to 0.81, slightly higher than those for Group II diorites (0.56–0.69). Moreover, amphibole Al^{IV} content shows positive correlations with Ti and $(Na + K)_A$, suggesting the composition was controlled by Ti-tschermark and edenite substitutions that are sensitive to crystallization temperature and pressure (Fig. 5b, c; Rutherford and Devine, 2003; Kiss et al., 2014). However, amphiboles in both groups of diorites show no relationship between Al^{IV} and Al^{VI} (Fig. 5d).

Low-Al amphiboles from both diorite groups have relatively consistent REE patterns that are slightly convex upward with Ce–Pr–Nd–Sm enrichment and distinctive negative Eu anomalies (Fig. 6a, c). On primitive mantle-normalized trace element diagrams, these amphibole grains show negative Pb, Sr, Eu, Zr, Hf, and Ti anomalies (Fig. 6b, d).

4.3. Whole-rock major and trace element compositions

Major and trace element data for the studied diorite samples are listed in Table S5. The Group I diorites have low SiO_2 contents (47.6–53.4 wt%) and high MgO contents (5.0–9.1 wt%) and $Mg^{\#}$ values (51–69). They have relatively high K_2O (1.0–3.6 wt%), Na_2O (1.7–3.4 wt%), and $Na_2O + K_2O$ (2.7–5.4 wt%) contents. They have variable Al_2O_3 (13.8–19.8 wt%), Fe_2O_3 (6.3–11.1 wt%), CaO (7.6–10.6 wt%) and low TiO_2 (0.59–1.28 wt%) contents. All of these rocks exhibit enrichment in LREE ($(La/Yb)_N$ = 5.7–10.5) with slightly negative Eu anomalies (δEu = 0.72–0.89) (Fig. 7a). On a primitive mantle-normalized trace element spider diagrams, they are enriched in large ion lithophile elements (LILEs; e.g., Pb, Rb, and Ba) and the depletion of high field strength elements (HFSEs; e.g., Nb and Ta). All these samples exhibit strong negative Nb, Ta, Ti, and P anomalies and positive Th anomalies (Fig. 7b).

The Group II diorites have relatively high contents of SiO_2 (56.9–59.5 wt%), Al_2O_3 (16.7–17.5 wt%), K_2O (0.7–2.4 wt%) and Na_2O (3.1–3.9 wt%). These rocks also contain relatively low contents of $Fe_2O_3^T$ (5.8–6.4 wt%), MgO (2.9–3.8 wt%), TiO_2 (0.77–0.81 wt%), and low $Mg^{\#}$ values (47–55). Chondrite-normalized REE patterns of the diorites exhibit LREE enrichment ($(La/Yb)_N$ = 8.9–10.4) and slightly negative Eu anomalies (δEu = 0.77–0.89) (Fig. 7a). In a primitive mantle-normalized trace element spider diagrams (Fig. 7b), the rocks are characterized by enrichment in LILEs (e.g., Rb, Ba, Th, and U) and depletion in HFSEs (e.g., Nb, Ta, Ti, P, Zr, and Hf), with positive Th and K anomalies and negative Nb, Ta, Ti, and P anomalies.

4.4. Whole-rock Sr—Nd isotopic compositions

Whole-rock Sr—Nd isotopic composition data for the diorites are listed in Table S6 and shown in Fig. 8a. The Group I diorites exhibit variable initial $^{87}Sr/^{86}Sr$ ratios (0.7073–0.7094) and negative $\varepsilon_{Nd}(t)$ values (−10.3 to −5.9) with single-stage Nd model ages (T_{Nd}^{DM}) ranging from 1.28 to 1.93 Ga. The Group II diorites show uniform initial $^{87}Sr/^{86}Sr$ ratios (0.7083–0.7087) and negative $\varepsilon_{Nd}(t)$ values (−9.5 to −9.0) with single-stage Nd model ages (T_{Nd}^{DM}) ranging from 1.59 to 1.69 Ga. The Sr − Nd isotopic compositions of these diorites are essentially similar to those arc magmas from the Daru Tso high-Mg andesites (Fig. 8a).

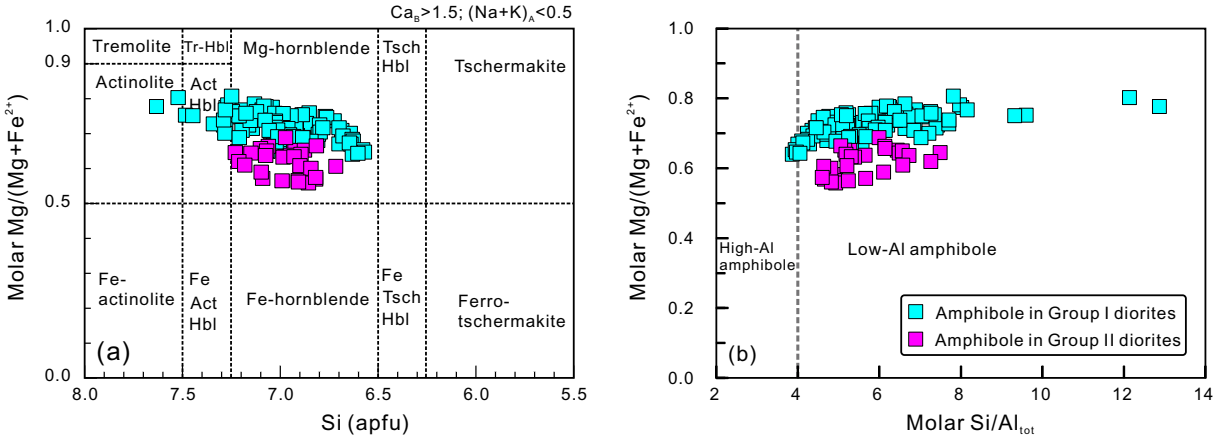

Fig. 4. Classification diagrams of (a) Si (apfu) versus Molar $Mg/(Mg + Fe^{2+})$ (Leake et al., 1997) and (b) Molar Si/Al_{tot} versus $Mg/(Mg + Fe^{2+})$ for amphibole from the Kenama diorites. Apfu = atom per formula unit.

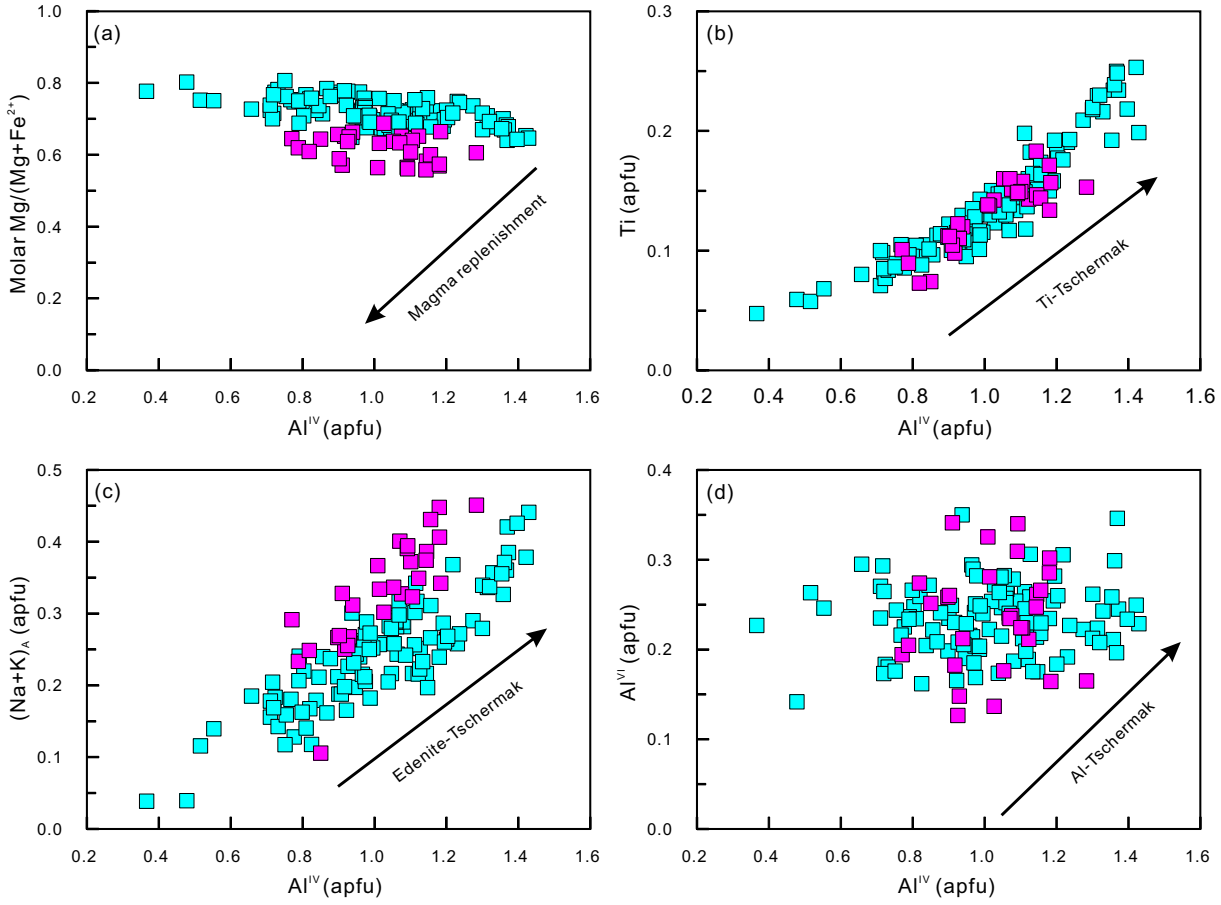

Fig. 5. Diagrams of Al^{IV} (apfu) versus Molar $Mg/(Mg + Fe^{2+})$ (a), Ti (apfu) (b), $(Na + K)_A$ (apfu) (c), and Al^{VI} (apfu) (d) illustrating the substitution mechanisms for the amphiboles from the Kenama diorites. Symbols are the same as in Fig. 4.

4.5. Zircon Hf—O isotopic compositions

Zircon in situ Hf—O isotope data for samples 16BG10–2, 16BG12–6, and 16BG12–10 are listed in Table S7 and shown in Fig. 8b. The measured $\delta^{18}O$ values for zircons from Group I diorite samples 16BG10–2 and 16BG12–6 have $\delta^{18}O$ values ranging from 6.9‰ to 7.3‰ (averaged of 7.1 ± 0.26‰, 2SD; Fig. 9a) and 6.5‰ to 7.2‰ (averaged of 6.75 ± 0.39‰, 2SD; Fig. 9c), respectively. The zircons $\delta^{18}O$ values from the Group II diorite sample 16BG12–10 vary from 6.6‰ to 7.5‰ (Fig. 9e), with an average of 7.0 ± 0.6‰ (2SD). The average zircon O isotope values for all samples are slightly higher than values for igneous zircons (5.3 ± 0.3‰) in equilibrium with mantle magmas (Valley et al., 2005).

Zircons from Group I diorite samples 16BG10–2 and 16BG12–6 have a large range of initial $^{176}Hf/^{177}Hf$ ratios of 0.282399–0.282548 and 0.282253–0.282534, corresponding to $\varepsilon_{Hf}(t)$ values of −9.7 to −4.4 and − 14.8 to −4.9 (Fig. 9b, d), respectively. They yield single-stage Hf model ages ranging from ca. 1.02 to 1.22 Ga and 1.09 to 1.44 Ga, respectively. The zircons from Group II diorite sample 16BG12–10 have a slightly wider range of initial $^{176}Hf/^{177}Hf$ ratios of 0.282381–0.282554, corresponding to $\varepsilon_{Hf}(t)$ values of −10.3 to −4.2 (Fig. 9f) and single-stage Hf model ages ranging from ca. 0.98 to 1.22 Ga.

5. Discussion

5.1. Crystallization conditions

Amphibole can be used to estimate crystallization conditions (Erdmann et al., 2014). Empirical and experimental studies have shown that amphibole compositions can be effectively used to estimate magma conditions during the crystallization of igneous rocks (e.g., Krawczynski et al., 2012; Ridolfi et al., 2010). Here, we constrain crystallization pressures, temperatures, H_2O_{melt} concentration, and oxygen fugacity for the Kenama magmas using the empirical amphibole formulation (Ridolfi et al., 2010). Amphiboles from the Kenama diorites plot inside the stability field of consistent amphiboles, indicating that they are suitable for determining crystallization conditions (Fig. 10). As illustrated in Figure S2, amphiboles in Group I diorites yield pressures of 131 ± 36 MPa, temperatures of 810 ± 30 °C H_2O_{melt} of 5.8 ± 0.4 wt%, which overlap the conditions of the low-Al amphiboles (121 ± 27 MPa, 797 ± 25 °C and 5.3 ± 0.3 wt%) in Group II diorite samples (Fig. 10a). Therefore, the amphibole from Kenama diorites crystallized under hydrous (H_2O = 4.6–6.9 wt%) and low-pressure (69–226 MPa) conditions that correspond to upper crustal depths and at temperatures of 745–871 °C. The results indicate that olivine and clinopyroxene may have crystallized prior to amphibole and separated from the residual magma.

5.2. Petrogenesis of the diorites

5.2.1. Crustal assimilation

Crustal contamination is an important process when mantle-derived magmas ascend through continental crust or stay within a crustal magma chamber, and may modify both elemental and isotopic compositions of magmas (e.g., Castillo et al., 1999; DePaolo, 1981). Given that crustal components are generally characterized by high $^{87}Sr/^{86}Sr$ and Rb/Sr ratios, and distinctly low $\varepsilon_{Nd}(t)$ and $\varepsilon_{Hf}(t)$ values and MgO contents (Rudnick and Fountain, 1995), any crustal contamination during magma ascent would have caused an increase in $(^{87}Sr/^{86}Sr)_i$ and a

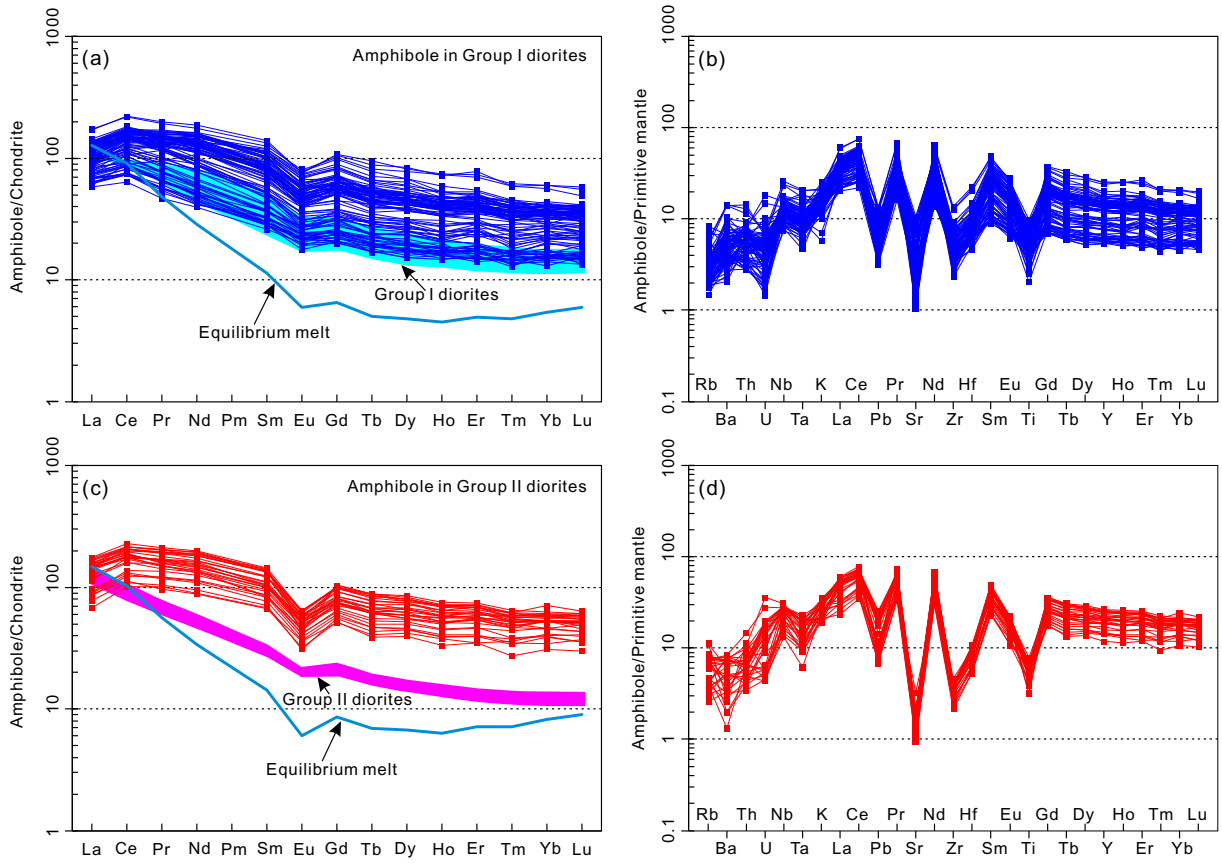

Fig. 6. (a, c) Chondrite-normalized REE patterns and (b, d) primitive mantle-normalized trace element spider diagrams for the amphiboles from the Kenama diorites. The normalization values for REE and trace elements are from Sun and McDonough (1989). The compositions of equilibrium melts are calculated by partition coefficients between amphibole and melt (Shimizu et al., 2017).

decrease in $\varepsilon_{Nd}(t)$ in the magma suites (Rogers et al., 2000). Although the Kenama diorites have high initial $^{87}Sr/^{86}Sr$ and negative zircon $\varepsilon_{Hf}(t)$ and whole-rock $\varepsilon_{Nd}(t)$ values, the absence of correlations of $(^{87}Sr/^{86}Sr)_i$, $\varepsilon_{Nd}(t)$ and $(Nb/La)_{PM}$ with MgO, SiO_2 and Rb/Sr are inconsistent with crustal contamination processes (Fig. 11a–g). Additionally, the Ce/Pb ratio does not decrease with the increase of SiO_2 content (Fig. 11h), indicating that no obvious crustal contamination. Therefore, crustal contamination played an insignificant role during the magma ascent. This is also supported by the absence of old inherited zircons form the Kenama diorites.

5.2.2. Fractional crystallization and accumulation

The variable major and trace element compositions of the Kenama diorites suggest that varying degrees of fractional crystallization and/or crystal accumulation possibly played an important role in their formation. In general, mantle-derived primary melts have Ni >400 ppm

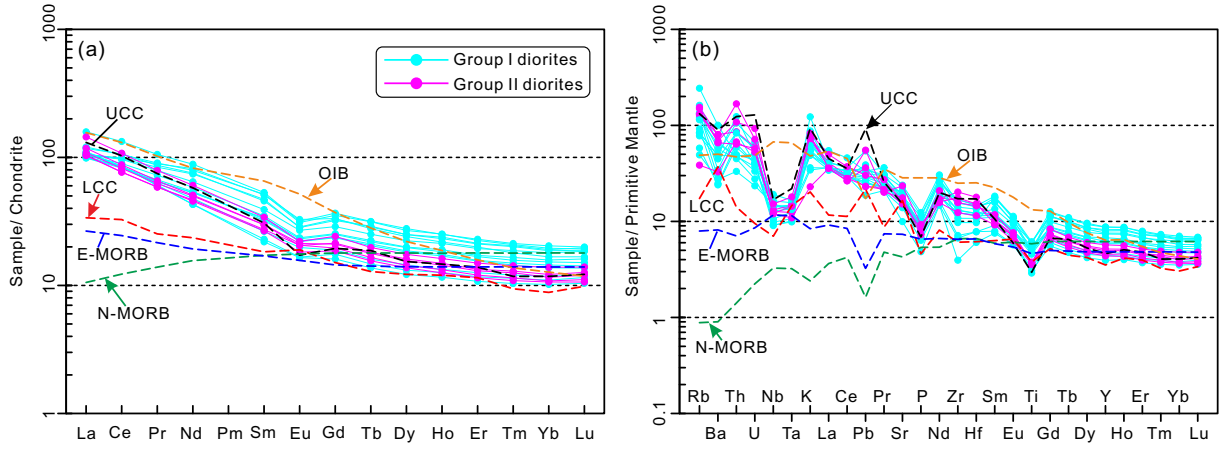

Fig. 7. (a) Chondrite-normalized REE patterns and (b) primitive mantle-normalized trace element spider diagrams for the Kenama diorites. Normalization values are from Sun and McDonough (1989). Data sources: OIB (Oceanic Island Basalt), N–MORB (Normal Mid–Ocean Ridge Basalt) and E–MORB (Enriched Mid–Ocean Ridge Basalt) are from Sun and McDonough (1989); upper and lower continental crust are from Rudnick and Gao (2003).

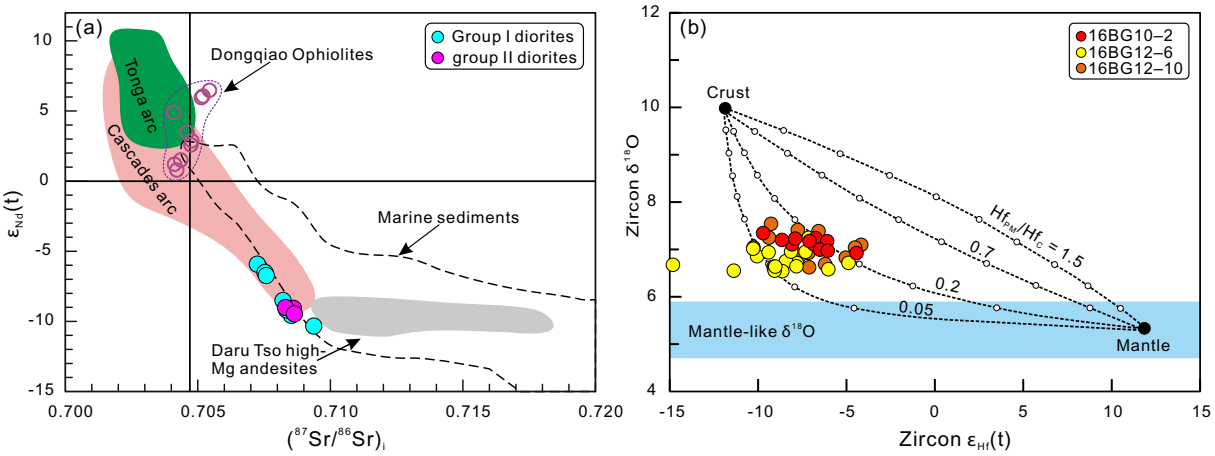

Fig. 8. (a) $\varepsilon_{Nd}(t)$ versus $(^{87}Sr/^{86}Sr)_i$ and (b) zircon $\varepsilon_{Hf}(t)$ versus $\delta^{18}O$ diagrams. The shaded field depicts $\delta^{18}O$ values of 5.3 ± 0.6‰ (2SD) for mantle–derived zircons (Valley et al., 1998). Hf_{pm}/Hf_c is the ratio of Hf concentration in the parental mantle magma (pm) to that in crustal (c) melt for each curve, and the small open circles on the curves represent 10% mixing increments by assuming mantle zircon with $\varepsilon_{Hf} = 12$ and $\delta^{18}O = 5.6‰$, and supracrustal zircon with $\varepsilon_{Hf} = -12$ and $\delta^{18}O = 10‰$. Data for Dongqiao Ophiolites are from Liu et al. (2016), sediments are from Plank and Langmuir (1998), Daru Tso high-Mg andesites are from Zeng et al. (2016), intermediate-basic volcanic rocks in the Cascades arc and Tonga arc are from GEOROC (http://georoc.mpch-mainz.gwdg.de/georoc/).

and Cr >1000 ppm (Wilson, 1989), and $Mg^{\#} = 73–81$ (Sharma, 1997). The Kenama diorite samples exhibit variable MgO concentrations and $Mg^{\#}$ values, suggesting that they underwent varying degrees of fractional crystallization. They show large variations in $Mg^{\#}$ values (47–69) and the contents of compatible elements such as Cr (5.18–629 ppm) and Ni (5.67–107.5 ppm). Their MgO contents are positively correlated with Cr and Ni contents (Figure S3h, i), indicating a significant fractionation of olivine and chromite. In addition, there is a well-defined positive correlation between CaO and MgO (Figure S3e), indicating clinopyroxene fractionation (Herzberg et al., 2007). The Kenama diorites show obvious negative Eu anomalies in a chondrite-normalized REE diagrams (Fig. 7), suggesting that plagioclase fractionation occurred during magma evolution. We further explore the fractional crystallization models using Rhyolite-MELTSs (Gualda and Ghiorso, 2015) with a starting composition of sample 16BG10–1. The modeling results indicate that fractional crystallization likely occurred along the liquid lines of descent of olivine, clinopyroxene, amphibole, feldspar and Fe—Ti oxides at lower pressure (1–2 kbar), ~4 wt% H_2O content and higher oxygen fugacity (NNO, NNO + 1, and NNO + 2) (Fig. 12). The Group I diorites have low SiO_2 (47.6–53.4 wt%), and high MgO (5.0–9.1 wt%), resulting from the accumulation of amphiboles.

5.2.3. Magma source characteristics

Various models have been proposed to explain the origin of intermediate igneous rocks, including (1) partial melting of mafic lower crust (e.g., Cai et al., 2015; Jung et al., 2002); (2) mixing between mantle-derived basaltic magma and crust-derived felsic melt (e.g., Guo et al., 2007; Reubi and Blundy, 2009; Streck et al., 2007; Zhang et al., 2013); (3) fractional crystallization of mantle-derived mafic magmas (e.g., Pichavant and Macdonald, 2007; Stevenson et al., 1999); and (4) interaction between slab-derived melts/fluids and mantle wedge (e.g., Shimoda et al., 1998; Tatsumi and Hanyu, 2003; Wang et al., 2008, 2011).

Experimental studies have shown that dehydration melting of crustal rocks (basaltic and pelitic) would produce low-$Mg^{\#}$ (generally <40) melts regardless of the degree of melting (Patiño Douce and Johnston, 1991; Rapp and Watson, 1995). The Group I diorites have high and variable $Mg^{\#}$ values of 51–69, indicating they were derived mainly from the mantle rather than the crustal material. The rocks show low SiO_2 (47.6–53.4 wt%) contents and variable MgO (5.0–9.10 wt%), Ni (5.7–107.5 ppm) and Cr (5.2–629.7 ppm) contents, suggesting they are products of evolved melts. Additionally, these diorites did not contain mafic microgranular enclaves and show similar Sr–Nd–Hf–O isotopic compositions (Figs. 8 and 9), indicating that magma mixing is not considered as a plausible mechanism accounting for their formation.

The negative zircon $\varepsilon_{Hf}(t)$ and whole-rock $\varepsilon_{Nd}(t)$ values and high initial $^{87}Sr/^{86}Sr$ ratios (Fig. 8) of the Kenama Group I diorites can be attributed either to melts derived from asthenospheric mantle with crustal contamination or from enriched lithospheric mantle. The Group I diorites are characterized by relative enrichment in LILEs, LREEs and U, and depletion in HFSEs (e.g., Nb, Ta, and Ti), indicating a typical arc-like geochemical affinities (Fig. 7b). Previous studies have demonstrated that slab-derived aqueous fluids contain high LILEs (Ba, Rb, Sr, U, and Pb) concentrations, whereas subducted oceanic sediment-derived melts contain high contents of Th and LREEs with distinctly elevated Th/Ce ratios (Hawkesworth et al., 1997). The Group I diorites have relatively high Th/Yb (0.92–4.50), Th/La (0.11–0.41), and La/Sm (3.20–7.58) ratios, and low Ba/La (6.7–24.6), Ba/Th (27.9–169.5), and U/Th (0.10–0.26) ratios, and they plot in the range of slab-derived melts on Ba/La versus Th/Yb and Ba/Th versus La/Sm diagrams (Fig. 13a, b). These results suggest lithospheric metasomatism was induced by sediment-derived melts (Plank, 2005; Woodhead et al., 2001). Moreover, the abundant amphiboles (Fig. 2c) as a hydrous mineral in the diorites, indicates that the Group I diorites were derived from a hydrous mantle source, as amphibole is stable under the conditions of lithospheric mantle, but not in convecting upper mantle or upwelling thermal mantle plumes (Class and Goldstein, 1997). The coeval high-Mg andesites in the Daru Tso (i.e., our study area) have similar geochemical and isotopic compositions to the Kenama diorites (Fig. 8), also suggesting that an enriched lithosphere mantle existed beneath the margin of the northern Lhasa subterrane during Jurassic times (Tang et al., 2019; Zeng et al., 2016). Therefore, the Group I diorites were most likely derived from enriched lithospheric mantle that had been metasomatized by subducted oceanic sediment-derived melts (e.g., Davidson, 1987; Hawkesworth et al., 1997; Zheng et al., 2015).

Oxygen isotopes are a powerful tool for determining the involvement of continental crustal materials in magma genesis, given the large difference in $\delta^{18}O$ between crustal rocks and mantle-derived rocks (James, 1981). Zircon is a generally robust and strongly refractory accessory mineral in igneous rocks. It is commonly accepted that the igneous fractionation has a negligible effect on the oxygen isotopic composition of zircon (Valley et al., 2005; Zheng et al., 2004). The zircons

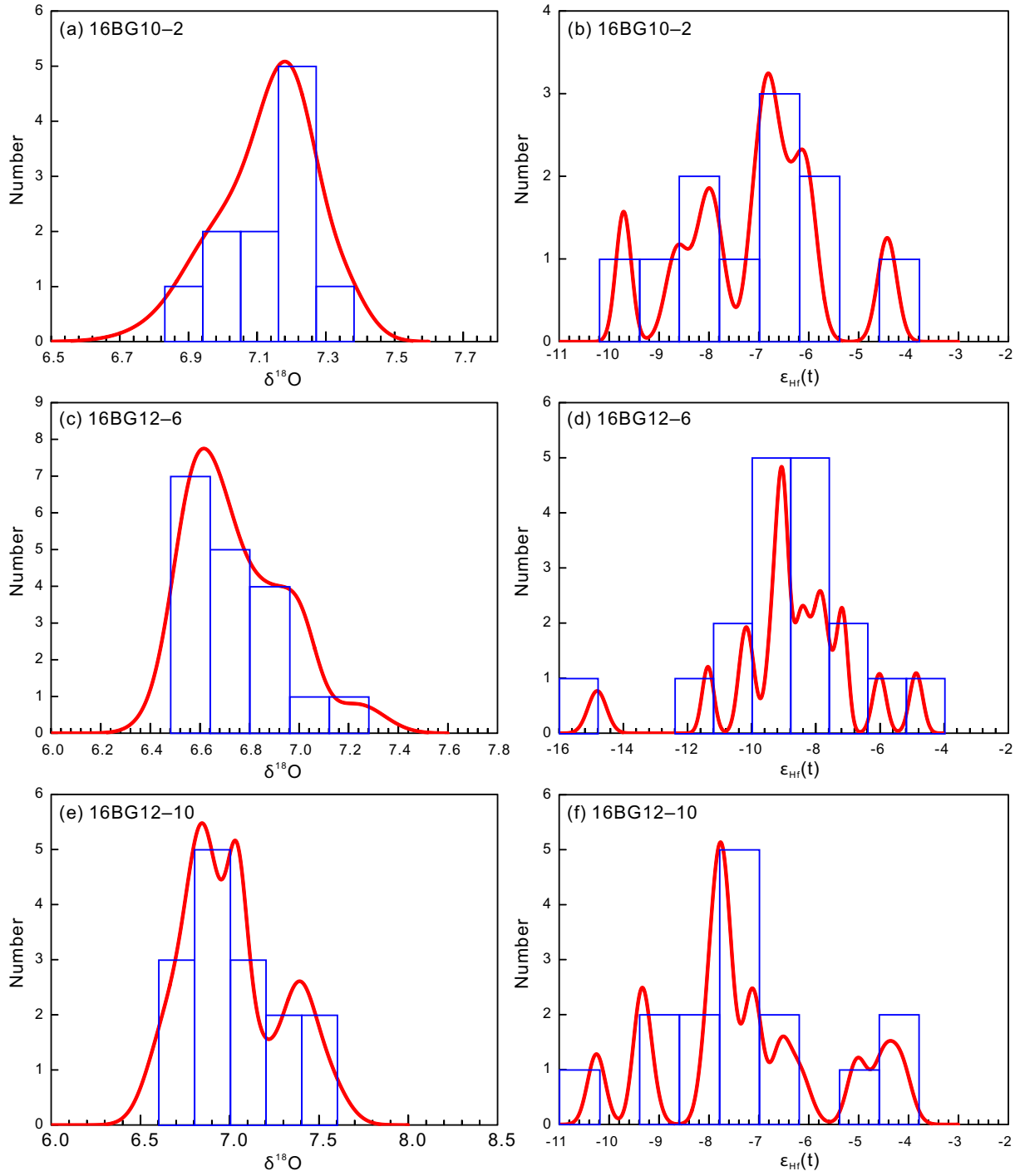

Fig. 9. Probability plots of zircon $\delta^{18}O$ and $\varepsilon_{Hf}(t)$ values for the Kenama diorites.

from the Kenama diorites show slightly high $\delta^{18}O$ (6.5‰ to 7.5‰) values relative to igneous zircons (5.3 ± 0.3‰) in equilibrium with mantle magmas (Valley et al., 2005) (Fig. 8b), suggesting that they contain an ^{18}O-enriched supracrustal component (e.g., a subducted oceanic sediment-derived melt) (Kemp et al., 2007; Turner et al., 2009). Therefore, we suggest that the parental magmas of these diorites originated from an enriched lithospheric mantle source that had been metasomatized by melts derived from the subducted oceanic slab with minor crustal contamination.

Compared with the Group I diorite samples, the Group II diorites have relatively high SiO_2, K_2O, and Na_2O contents, and low TiO_2, CaO, $Fe_2O_3^T$, MgO, Cr, and Ni contents (Figure S3). The Group II diorites display similar chondrite-normalized REE and primitive mantle-normalized trace element patterns to the Group I diorites (Fig. 7), suggesting that they were formed by fractional crystallization of similar parental magmas. The Group II diorites exhibit negative zircon $\varepsilon_{Hf}(t)$ (−10.25 to −4.16) values, elevated $\delta^{18}O$ values (6.62‰ to 7.54‰), low $\varepsilon_{Nd}(t)$ values (−9.5 to −9.0), and high initial $^{87}Sr/^{86}Sr$ ratios (0.7083–0.7087) of whole rock, also similar to the Group I diorites (Fig. 8). Therefore, the Group II diorites were also sourced from an enriched lithospheric mantle metasomatized by subduction-related sediment melts.

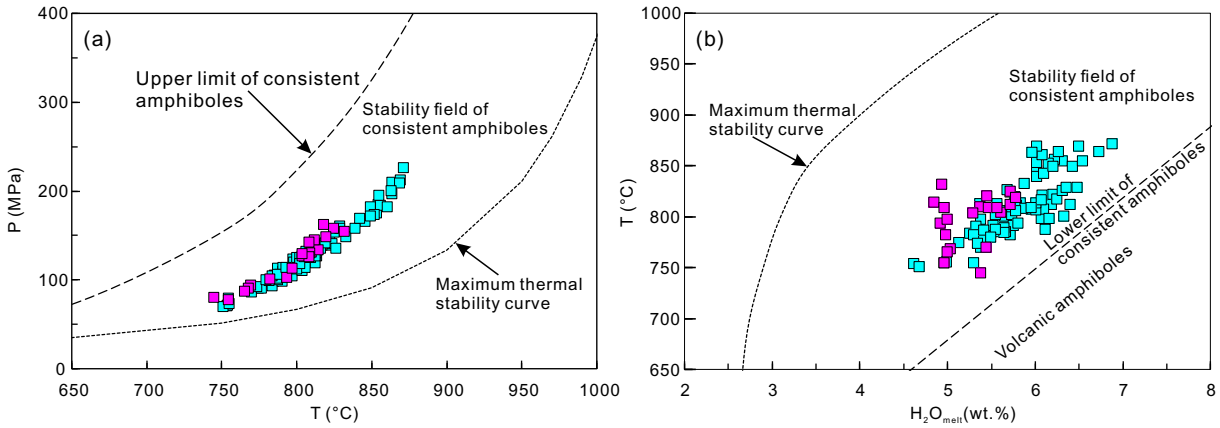

Fig. 10. (a) P–T and (b) T–H_2O_{melt} diagrams for the amphiboles from the Kenama diorites. Pressure, temperature, and H_2O_{melt} concentration of the Kenama diorites were determined using the empirical amphibole formulation (Ridolfi et al., 2010). Symbols are the same as in Fig. 4.

5.3. Role of amphibole fractionation in arc magmas

Amphiboles are common hydrous minerals in magmatic rocks. The textures and compositions of amphibole crystals have been utilized to infer magmatic processes and crystallization parameters (Chelle-Michou and Chiaradia, 2017; Davidson et al., 2007). Amphiboles from the two groups of diorites are typically characterized by low Al^{IV} (0.37–1.43; Fig. 4b) and low crystallization temperatures (~871–745 °C; Fig. 10), suggesting they were derived from a cold silicic magma (Chambefort et al., 2013; Kiss et al., 2014; Ridolfi et al., 2010). Meanwhile, the amphiboles of both diorite groups show similar compositional trends on Al_2O_3 versus TiO_2, CaO, Na_2O, and Cl diagrams (Figure S1b, e, f, and h), indicating crystallization from a single magma source. The weak negative correlation between Al^{IV} and $Mg^{\#}$ (Fig. 5a) indicates the absence of mafic magma replenishment (Kiss et al., 2014; Ridolfi et al., 2010). Negative Eu anomalies and depletion in Sr, Zr and, Ti (Fig. 6b, d) indicate that the amphiboles were formed after plagioclase and magnetite crystallization (Chambefort et al., 2013; Coint et al., 2013; Kiss et al., 2014; Krawczynski et al., 2012). Moreover, based on partition coefficients between amphibole and melt (Shimizu et al., 2017), the calculated equilibrium melts show lower REE compositions than the host diorites, possibly suggesting that the amphibole crystallized at an early stage.

To better assess the role of mineral fractionation in arc magmatism, we investigated the relationships between major- and trace- element variations in the amphiboles. Notably, the increase in Dy and Eu concentrations with increasing Dy/Yb ratio, suggests that the differentiation of deep magmas in the Kenama area was dominated by the fractionation of amphiboles (Fig. 14a, b). Moreover, Ti concentrations in the amphibole crystals broadly correlate with their Dy/Yb ratios (Fig. 14c), suggesting that the deep magmas evolved towards lower Ti concentrations by fractional crystallization of amphiboles (Peters et al., 2017). In addition, the Eu/Eu* ratio of the amphiboles increase with their $Mg^{\#}$ values, suggesting that the parent magmas of the amphiboles may have evolved towards lower Eu and $Mg^{\#}$ by progressive fractionation of amphibole and/or feldspar (Fig. 14d).

Therefore, we suggest that both groups of Kenama diorites probably originated from an enriched lithospheric mantle metasomatized by subducted oceanic sediment-derived melts. Their parental magmas may have similar geochemical characteristics and underwent varying degrees of accumulation and fractional crystallization. The Group I diorites were likely generated by accumulation of amphibole and fractional crystallization of olivine, clinopyroxene, and plagioclase from mafic magmas. Instead, the group II diorites were formed by fractional crystallization of clinopyroxene and plagioclase from mafic magmas that were geochemically similar to the Group I diorites.

5.4. Geodynamic implications

The tectonic setting of the Jurassic–Cretaceous magmatic rocks in the BNSZ is debated, with previous studies proposing an island arc setting (Li et al., 2018; Liu et al., 2016; Wang et al., 2016; Zeng et al., 2016; Zhu et al., 2016; Zhu et al., 2017, 2019a) or a post-collisional setting (Ma et al., 2017; Yan et al., 2016). The debate stems from insufficient petrogenetic constrains on the Jurassic mafic-intermediate magmatic rocks, as well as a lack of synthetic comparison of magmatic activity with other geological records.

Ma et al. (2017) proposed that the Lhasa–Qiangtang collision took place in late Middle Jurassic time (166 Ma), based on the field observation of an angular unconformity that truncated the Jurassic succession and the recognition of siliciclastic provenance changed from arc magmatic sources to uplifted orogenic sources in the Biluoco–Qixiangco area from the southern Qiangtang basin. However, many researchers suggest an oceanic subduction tectonic setting for the BNSZ during the Jurassic time. The lines of evidence for subduction and closure of the BNTO are as follows: (1) High-magnesium andesitic rocks have been identified in the Daru Tso and Jiaqiong areas in the middle-eastern segment of the BNSZ. These high-magnesium andesitic rocks were derived from interaction between partial melting of subducted sediments and overlying mantle peridotite, and formed in an arc setting related to the subduction of the Bangong–Nujiang Tethys oceanic lithosphere (Tang et al., 2019; Zeng et al., 2016); (2) Sedimentary provenance and age-spectra of detrital zircons of the Early Cretaceous strata (Duba and Duoni Formations) from our study area indicate that the Lhasa–Qiangtang collision took place during the late Early Cretaceous (~122–113 Ma) (Lai et al., 2019; Zhu et al., 2019b); (3) To the west of the study area in the Nyima basin, major deformation and denudation occurred at ca. 125–118 Ma, resulting in an evolution from marine to nonmarine environments (Kapp et al., 2007). This indicates that the Lhasa–Qiangtang collision was well underway in the Early Cretaceous; (4) Farther to the west in Domar within the southern Qiangtang subterrane, structural mapping and detrital zircon U—Pb dating indicated a significant Late Jurassic–Early Cretaceous shortening (Raterman et al., 2014); (5) Jurassic–Early Cretaceous ophiolite fragments were widely distributed along the BNSZ (Fig. 1b; Wang et al., 2016), and generated in a fore-arc oceanic setting (Liu et al., 2016; Wang et al., 2016). The ages of these ophiolites indicate that the BNTO still exists during the Early Cretaceous (Wang et al., 2016; Zhong et al., 2017); and (6) Paleomagnetic results of the Middle Jurassic limestones from the Shuanghu area in the southern Qiangtang terrane indicate that the width of the BNTO was 2600 ± 710 km (23.4° ± 6.4°) during the Middle Jurassic, and the closure of BNTO occurred in the Cretaceous (Cao et al., 2019).

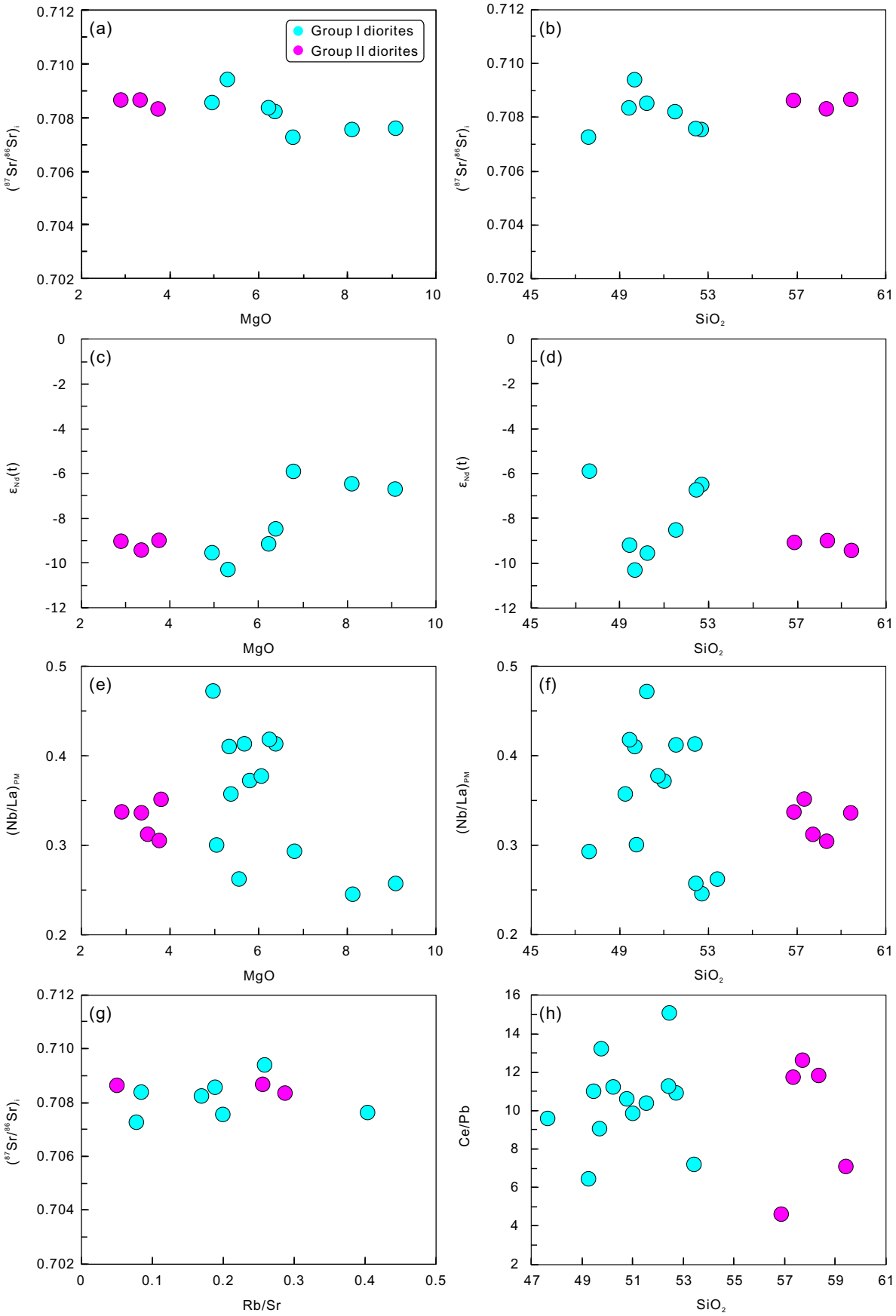

Fig. 11. Diagrams of MgO versus $(^{87}Sr/^{86}Sr)_i$ (a), SiO_2 versus $(^{87}Sr/^{86}Sr)_i$ (b), MgO versus $\varepsilon_{Nd}(t)$ (c), SiO_2 versus $\varepsilon_{Nd}(t)$ (d), MgO versus $(Nb/La)_{PM}$ (e), SiO_2 versus $(Nb/La)_{PM}$ (f), Rb/Sr versus $(^{87}Sr/^{86}Sr)_i$ (g) and SiO_2 versus Ce/Pb (h).

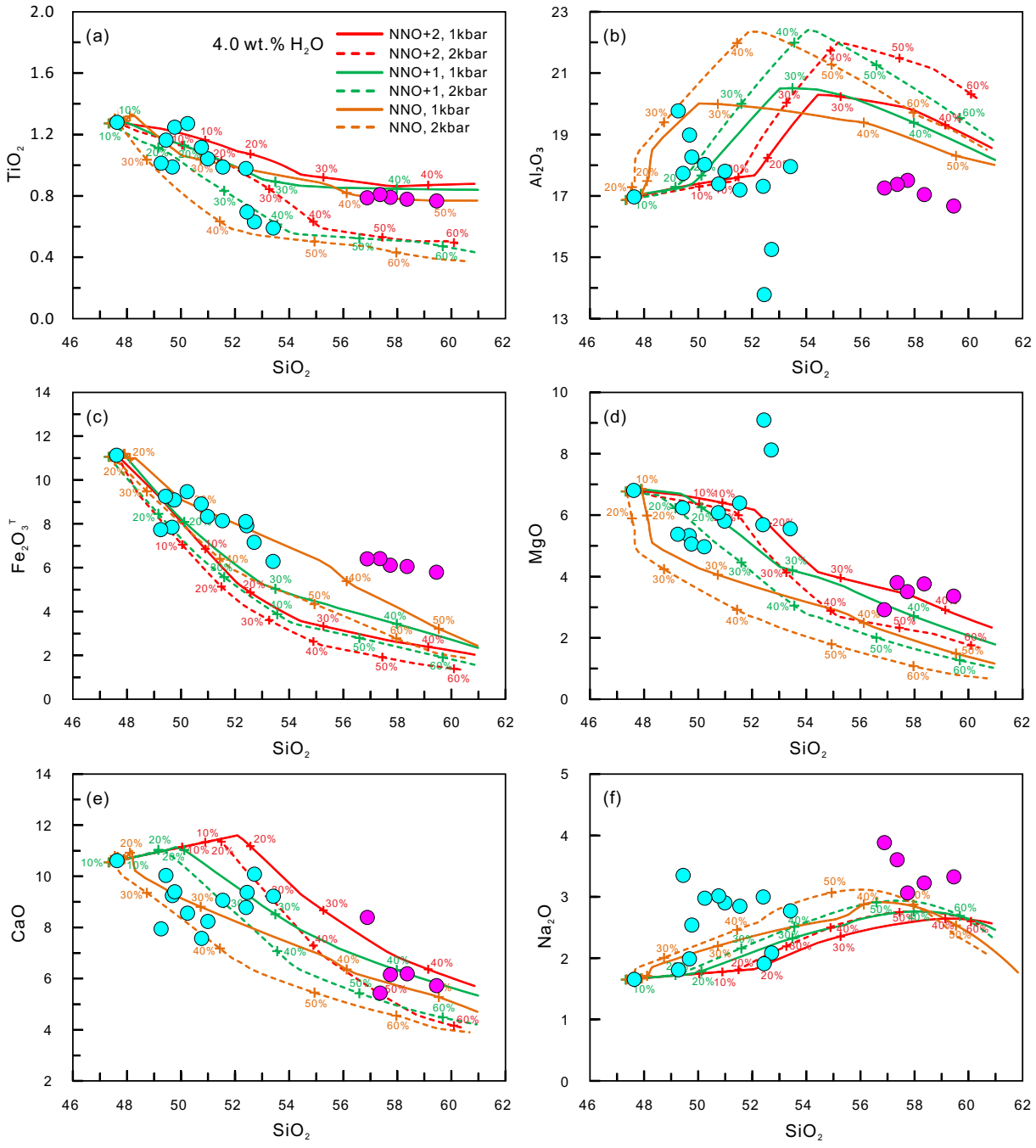

Fig. 12. Chemical variations and fractionation models of diorites from the Kenama area. Rhyolite-MELTS fractionation models of a starting composition of sample 16BG10–1 are given at lower pressure (1–2 kbar), ~4 wt% H_2O content, and higher oxygen fugacities (NNO, NNO + 1 and NNO + 2). Tick marks at 10% intervals represent the percentage of crystallization. Symbols are the same as in Fig. 11.

The early Late Jurassic Kenama diorites of our study have recently been discovered in the Kenama area along the southern margin of the BNSZ. The U—Pb ages of these diorites are consistent with the high-magnesium andesitic rocks (~165–161 Ma) that identified in the Daru Tso and Jiaqiong areas in the middle-eastern segment of the BNSZ (Tang et al., 2019; Zeng et al., 2016). In addition, previous studies indicate that ophiolitic mélange in the Dongqiao–Lanong area is Jurassic in age (i.e., our study area) (Wang et al., 2016). The Dongqiao and Lanong ophiolites were produced during the Early Jurassic (~188 Ma; Liu et al., 2016) and Late Jurassic (~147 Ma; Zhong et al., 2017), respectively. All these ophiolites were formed in a fore-arc oceanic setting and indicate that the BNTO, in particular its middle and eastern segments, were not closed until the Late Jurassic (Liu et al., 2016; Wang et al., 2016; Zhong et al., 2017). The Kenama diorites have the geochemical characteristics of typical arc-like rocks and were derived from a lithospheric mantle source that had been metasomatized by sediment melts of the subducted oceanic slab. In combination with regional geology, in particular adjacent ophiolites, high-magnesian andesitic rocks and Cretaceous sedimentary rocks, we suggest that all of the Kenama diorites were formed in an early Late Jurassic arc setting related to the subduction of

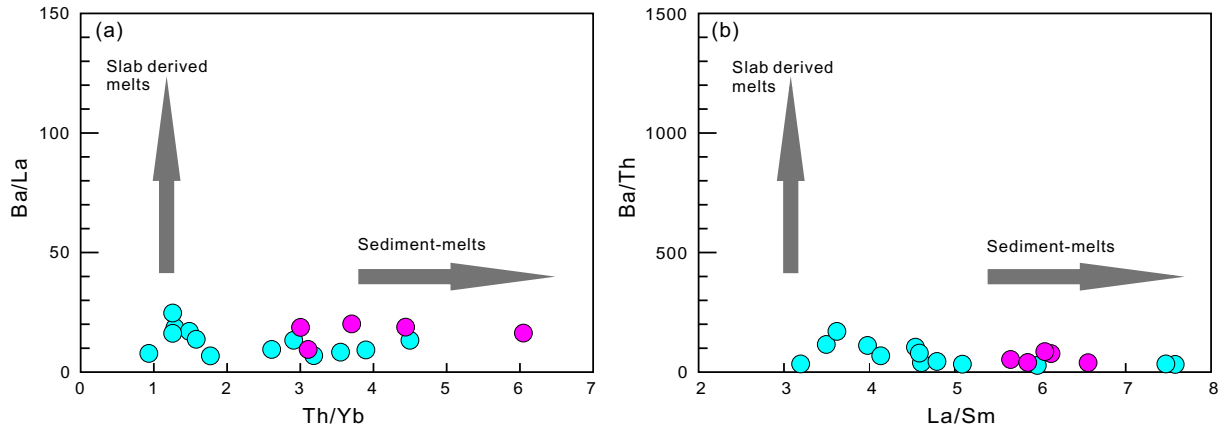

Fig. 13. (a) Ba/La versus Th/Yb and (b) Ba/Th versus La/Sm diagrams for the Kenama diorites. Symbols are the same as in Fig. 11.

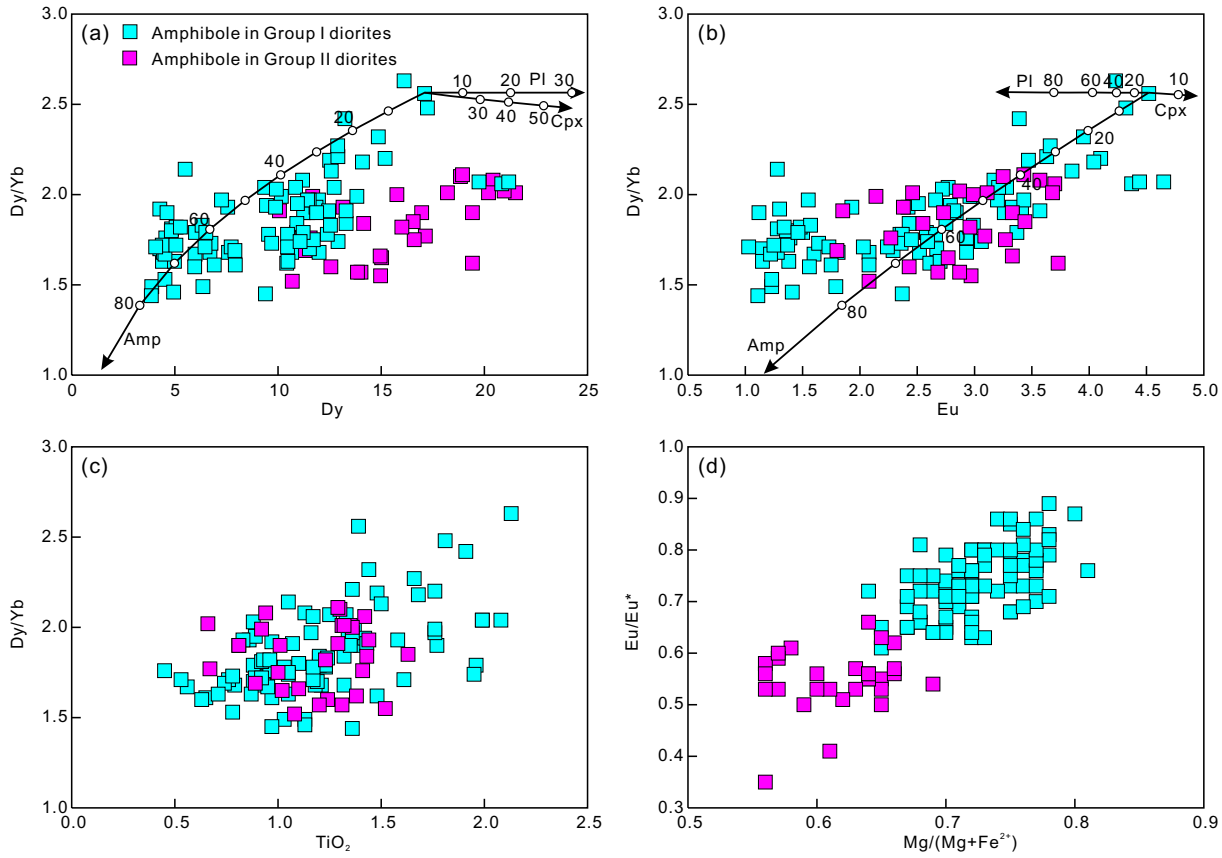

Fig. 14. Major and trace element variations within amphiboles from the Kenama diorites.

the Bangong–Nujiang Tethys oceanic lithosphere. This result is also consistent with paleomagnetic data of the Middle Jurassic limestones from the Shuanghu area in the southern Qiangtang Terrane (Cao et al., 2019).

6. Conclusions

(1) New SIMS and LA–ICP–MS zircon U—Pb dating results suggest that the Kenama diorites were formed during the early Late Jurassic (162–159 Ma).

(2) Amphiboles from Group I and II diorites have low Al_2O_3 contents and were formed under conditions of 751–871 °C and 69–226 Mpa (Group I) and 745–832 °C and 77–162 Mpa (Group II). Distinctive negative Eu anomalies and negative anomalies in Pb, Sr, Eu, Zr, Hf, and Ti suggest that these amphiboles crystallized from arc magma that had previously crystallized plagioclase and magnetite.

(3) Geochemical and isotopic characteristics suggest that both groups of Kenama diorites originated from an enriched lithospheric mantle metasomatized by subducted sediment-derived melts. Their parental magmas may have similar geochemical characteristics and underwent varying degrees of accumulation and fractional crystallization. The Group I diorites were generated by accumulation of amphibole and fractional crystallization of olivine, clinopyroxene, and plagioclase from mafic magmas,

and Group II diorites were formed by the fractional crystallization of olivine, clinopyroxene, and plagioclase from mafic magmas that were geochemically similar to the Group I diorites. All of the Kenama diorites were generated in an early Late Jurassic arc setting that resulted from subduction of the Bangong–Nujiang Tethys oceanic lithosphere.

Declaration of Competing Interest

The authors declare that they have no known competing financial interests or personal relationships that could have appeared to influence the work reported in this paper.

Acknowledgments

We thank Editor-in Chief Professor Greg Shellnutt, Professor Shao-Cong Lai, and three anonymous reviewers for their constructive and helpful comments on the manuscript. We also appreciate the assistance of Xiao-Ping Xia, Le Zhang, Sheng-Ling Sun, Xiang-Lin Tu, Xin-Yu Wang, Wen Zeng and Lin-Li Chen for zircon dating and Hf—O isotopic, whole-rock and mineral geochemical analyses. Financial support for this research was provided by the Strategic Priority Research Program (A) of the Chinese Academy of Sciences (grant no. XDA2007030402), the National Natural Science Foundation of China (41630208 and 91855215), the Second Tibetan Plateau Scientific Expedition and Research (STEP) (2019QZKK0702), the National Key R & D Program of China (2016YFC0600407), the Key Program of the Chinese Academy of Sciences (QYZDJ-SSW-DQC026) and the Guangzhou Institute of Geochemistry, Chinese Academy of Science (GIGCAS 135 project 135TP201601). This is contribution No. IS-2878 from GIGCAS.

Appendix A. Supplementary data

Supplementary data to this article can be found online at https://doi.org/10.1016/j.lithos.2020.105644.

References

Brown, M., 2013. Granite: from genesis to emplacement. Geol. Soc. Am. Bull. 125, 1079–1113.

Cai, Y.F., Wang, Y.J., Cawood, P.A., Zhang, Y.Z., Zhang, A.M., 2015. Neoproterozoic crustal growth of the Southern Yangtze Block: geochemical and zircon U-Pb geochronological and Lu-Hf isotopic evidence of neoproterozoic diorite from the Ailaoshan zone. Precambrian Res. 266, 137–149.

Cao, Y., Sun, Z., Li, H., Pei, J., Liu, D., Zhang, L., Ye, X., Zheng, Y., He, X., Ge, C., Jiang, W., 2019. New paleomagnetic results from Middle Jurassic limestones of the Qiangtang terrane, Tibet: Constraints on the evolution of the Bangong–Nujiang Ocean. Tectonics 38, 215–232.

Cao, Y., Sun, Z., Li, H., Ye, X., Pan, J., Liu, D., Zhang, L., Wu, B., Cao, X., Liu, C., Yang, Z., 2020. Paleomagnetism and U-Pb Geochronology of Early Cretaceous Volcanic Rocks from the Qiangtang Block. Implications for the Qiangtang-Lhasa Collision, Tectonophysics, Tibetan Plateau https://doi.org/10.1016/j.tecto.2020.228500.

Castillo, P.R., Janney, P.E., Solidum, R.U., 1999. Petrology and geochemistry of Camiguin Island, southern Philippines: insights to the source of adakites and other lavas in a complex arc setting. Contrib. Mineral. Petrol. 134, 33–51.

Chambefort, I., Dilles, J.H., Longo, A.A., 2013. Amphibole geochemistry of the Yanacocha volcanics, Peru: evidence for diverse sources of magmatic volatiles related to gold ores. J. Petrol. 54, 1017–1046.

Chelle-Michou, C., Chiaradia, M., 2017. Amphibole and apatite insights into the evolution and mass balance of Cl and S in magmas associated with porphyry copper deposits. Contrib. Mineral. Petrol. 172, 105.

Class, C., Goldstein, S.L., 1997. Plume–lithosphere interactions in the ocean basins: constrains from the source mineralogy. Earth Planet. Sci. Lett. 150, 245–260.

Coint, N., Barnes, C.G., Yoshinobu, A.S., Barnes, M.A., Buck, S., 2013. Use of trace element abundances in augite and hornblende to determine the size, connectivity, timing, and evolution of magma batches in a tilted batholith. Geosphere 9, 1747–1765.

Davidson, J., Turner, S., Handley, H., Macpherson, C., Dosseto, A., 2007. Amphibole "sponge" in arc crust? Geology 35, 787–790.

Davidson, J.P., 1987. Crustal contamination versus subduction zone enrichment: examples from the Lesser Antilles and implications for mantle source compositions of island arc volcanic rocks. Geochim. Cosmochim. Acta 51, 2185–2198.

Davidson, J.P., Hora, J.M., Garrison, J.M., Dungan, M.A., 2005. Crustal forensics in arc magmas. J. Volcanol. Geotherm. Res. 140, 157–170.

DePaolo, D.J., 1981. Trace element and isotopic effects of combined wallrock assimilation and fractional crystallization. Earth Planet. Sci. Lett. 53, 189–202.

Erdmann, S., Martel, C., Pichavant, M., Kushnir, A., 2014. Amphibole as an archivist of magmatic crystallization conditions: problems, potential, and implications for inferring magma storage prior to the paroxysmal 2010 eruption of Mount Merapi, Indonesia. Contrib. Mineral. Petrol. 167, 1016.

Fan, J.J., Li, C., Liu, Y.M., Xu, J.X., 2015a. Age and nature of the late early cretaceous Zhaga formation, northern Tibet: constraints on when the Bangong–Nujiang Neo-tethys Ocean closed. Int. Geol. Rev. 57, 342–353.

Fan, J.J., Li, C., Xie, C.M., Wang, M., Chen, J.W., 2015b. The evolution of the Bangong–Nujiang Neo-Tethys Ocean: evidence from zircon U–Pb and Lu–Hf isotopic analyses of early cretaceous oceanic islands and ophiolites. Tectonophysics 655, 27–40.

Fan, J.J., Li, C., Wang, M., Xie, C.M., 2017. Reconstructing in space and time the closure of the middle and western segments of the Bangong–Nujiang Tethyan Ocean in the Tibetan plateau. Int. J. Earth Sci. 107, 231–249.

Gualda, G.A.R., Ghiorso, M.S., 2015. MELTS_Excel: a Microsoft Excel-based MELTS interface for research and teaching of magma properties and evolution. Geochem. Geophys. Geosyst. 16, 315–324.

Guo, F., Nakamuru, E., Fan, W.M., Kobayoshi, K., Li, C.W., 2007. Generation of Palaeocene adakitic andesites by magma mixing, Yanji Area, NE China. J. Petrol. 48, 661–692.

Guynn, J., Kapp, P., Gehrels, G.E., Ding, L., 2012. U–Pb geochronology of basement rocks in Central Tibet and paleogeographic implications. J. Asian Earth Sci. 43, 23–50.

Guynn, J.H., Kapp, P., Pullen, A., Gehrels, G.E., Heizler, M., Ding, L., 2006. Tibetan basement rocks near Amdo reveal "missing" Mesozoic tectonism along the Bangong suture, Central Tibet. Geology 34, 505–508.

Hao, L.L., Wang, Q., Wyman, D.A., Ou, Q., Dan, W., Jiang, Z.Q., Wu, F.Y., Yang, J.H., Long, X.P., Li, J., 2016. Underplating of basalticmagmas and crustal growth in a continental arc: evidence from late Mesozoic intermediate–felsic intrusive rocks in southern Qiangtang, Central Tibet. Lithos 245, 223–242.

Hao, L.L., Wang, Q., Zhang, C.F., Ou, Q., Yang, J.H., Dan, W., Jiang, Z.Q., 2019. Oceanic plateau subduction during closure of the Bangong-Nujiang Tethyan Ocean: insights from central Tibetan volcanic rocks. Geol. Soc. Am. Bull. 131, 864–880.

Hawkesworth, C.J., Turner, S.P., McDermott, F., Peate, D.W., van Calsteren, P., 1997. U–Th isotopes in arc magmas: implications for element transfer from the subducted crust. Science 276, 551–555.

Hawthorne, F.C., Oberti, R., 2007. Classification of the amphiboles. Rev. Mineral. Geochem. 67, 55–88.

Herzberg, C., Asimow, P.D., Arndt, N., Niu, Y., Lesher, C.M., Fitton, J.G., Cheadle, M.J., Saunders, A.D., 2007. Temperatures in ambient mantle and plumes: constraints from basalts, picrites, and komatiites. Geochem. Geophys. Geosyst. 8, Q02006.

Hoskin, P.W., Schaltegger, U., 2003. The composition of zircon and igneous and metamorphic petrogenesis. Rev. Mineral. Geochem. 53, 27–62.

Huang, X.L., Xu, Y.G., Lo, C.H., Wang, R.C., Lin, C.Y., 2007. Exsolution Lamellae in a Clinopyroxene Megacryst Aggregate from Cenozoic Basalt, Leizhou Peninsula, South China: Petrography and Chemical Evolution. Contrib. Mineral. Petrol. 154, 691–705.

James, D.E., 1981. The combined use of oxygen and radiogenic isotopes as indicators of crustal contamination. Annu. Rev. Earth Planet. Sci. 9, 311–344.

Jones, R.E., Kirstein, L.A., Kasemann, S.A., Dhuime, B., Elliott, T., Litvak, V.D., Alonso, R., Hinton, R., Facility, E.I.M., 2015. Geodynamic controls on the contamination of Cenozoic arc magmas in the southern Central Andes: Insights from the O and Hf isotopic composition of zircon. Geochim. Cosmochim. Acta 164, 386–402.

Jung, S., Hoernes, S., Mezger, K., 2002. Synorogenic melting of mafic lower crust: constraints fromgeochronology, petrology and Sr, Nd, Pb and O isotope geochemistry of quartz diorites (Damara orogen, Namibia). Contrib. Mineral. Petrol. 143, 551–566.

Kapp, P., DeCelles, P.G., Gehrels, G.E., Heizler, M., Ding, L., 2007. Geological records of the Lhasa–Qiangtang and Indo-Asian collisions in the Nima area of Central Tibet. Geol. Soc. Am. Bull. 119, 917–932.

Kelemen, P.B., Hanghøj, K., Greene, A.R., 2014. 4.21 – one viewof the geochemistry of subduction-related magmatic arcs, with an emphasis on primitive andesite and lower crust. In: Rudnick, R.L., The Crust, Holland, H.D, Turekian, K.K. (Eds.), Treatise on Geochemistry, second ed. Elsevier, Oxford, pp. 749–806.

Kemp, A.I.S., Hawkesworth, C.J., Foster, G.L., Paterson, B.A., Woodhead, J.D., Hergt, J.M., Gray, C.M., 2007. Magmatic and crustal differentiation history of granitic rocks from Hf–O isotopes in zircon. Science 315, 980–983.

Kiss, B., Harangi, S., Ntaflos, T., Mason, P.R.D., Pál-Molnár, E., 2014. Amphibole perspective to unravel pre-eruptive processes and conditions in volcanic plumbing systems beneath intermediate arc volcanoes: a case study from Ciomadul volcano (SE Carpathians). Contrib. Mineral. Petrol. 167, 986–1519.

Krawczynski, M.J., Grove, T.L., Behrens, H., 2012. Amphibole stability in primitive arc magmas: effects of temperature, H_2O content, and oxygen fugacity. Contrib. Mineral. Petrol. 164, 317–339.

Lai, W., Hu, X., Garzanti, E., Xu, Y., Ma, A., Li, W., 2019. Early cretaceous sedimentary evolution of the northern Lhasa terrane and the timing of initial Lhasa-Qiangtang collision. Gondw. Res. 73, 136–152.

Leake, B.E., Woolley, A.R., Arps, C.E.S., Birch, W.D., Gilbert, M.C., Grice, J.D., Hawthorne, F.C., Kato, A., Kisch, H.J., Krivovichev, V.G., Linthout, K., Laird, J., Mandarino, J.A., Maresch, W.V., Nickel, E.H., Rock, N.M.S., Schumacher, J.C., Smith, D.C., Stephenson, N.C.N., Ungaretti, L., Whittaker, E.J.W., Guo, Y.Z., 1997. Report nomenclature of amphiboles: report of the subcommittee on amphiboles of the international mineralogical association commission on new minerals and mineral names. Mineral. Mag. 61, 1019–1037.

Li, J.X., Qin, K.Z., Li, G.M., Richards, J.P., Zhao, J.X., Cao, M.J., 2014. Geochronology, geochemistry, and zircon Hf isotopic compositions of Mesozoic intermediate–felsic intrusions in Central Tibet: petrogenetic and tectonic implications. Lithos 198–199, 77–91.

Li, S., Yin, C., Guilmette, C., Ding, L., Zhang, J., 2019. Birth and demise of the Bangong-Nujiang Tethyan Ocean: a review from the Gerze area of Central Tibet. Earth Sci. Rev. 198, 1–25.

Li, X.H., Sun, M., Wei, G.J., Liu, Y., Lee, C.Y., Malpas, J., 2000. Geochemical and Sm-Nd isotopic study of amphibolites in the Cathaysia Block, southeastern China: evidence for an extremely depleted mantle in the Paleoproterozoic. Precambrian Res. 102, 251–262.

Li, X.H., Zhou, H., Chung, S.L., Lo, C.H., Wei, G., Liu, Y., Lee, C.Y., 2002. Geochemical and Sr-Nd isotopic characteristics of late Paleogene ultrapotassic magmatism in southeastern Tibet. Int. Geol. Rev. 44, 559–574.

Li, X.H., Liu, D.Y., Sun, M., Li, W.X., Liang, X.R., Liu, Y., 2004. Precise Sm-Nd and U-Pb isotopic dating of the supergiant Shizhuyuan polymetallic deposit and its host granite, Southeast China. Geol. Mag. 141, 225–231.

Li, X.H., Qi, C.S., Liu, Y., Liang, X.R., Tu, X.L., Xie, L.W., Yang, Y.H., 2005. Petrogenesis of the Neoproterozoic bimodal volcanic rocks along the western margin of the Yangtze Block: new constraints from Hf isotopes and Fe/Mn ratios. Chin. Sci. Bull. 50, 2481–2486.

Li, X.H., Liu, Y., Li, Q.L., Guo, C.H., Chamberlain, K.R., 2009. Precise determination of Phanerozoic zircon Pb/Pb age by multicollector SIMS without external standardization. Geochem. Geophys. Geosyst. 10, Q04010. https://doi.org/10.1029/2009GC002400.

Li, X.H., Li, W.X., Li, Q.L., Wang, X.C., Liu, Y., Yang, Y.H., 2010a. Petrogenesis and tectonic significance of the ~850 Ma Gangbian alkaline complex in South China: evidence from in situ zircon U–Pb dating, Hf–O isotopes and whole-rock geochemistry. Lithos 114, 1–15.

Li, X.H., Long, W.G., Li, Q.L., Liu, Y., Zheng, Y.F., Yang, Y.H., Chamberlain, K.R., Wan, D.F., Guo, C.H., Wang, X.C., 2010b. Penglai zircon megacrysts: a potential new working reference material for microbeam determination of Hf–O isotopes and U–Pb age. Geostand. Geoanal. Res. 34, 117–134.

Li, X.H., Tang, G.Q., Gong, B., Yang, Y.H., Hou, K.J., Hu, Z.C., Li, Q.L., Liu, Y., Li, W.X., 2013. Qinghu zircon: a working reference for microbeam analysis of U-Pb age and Hf and O isotopes. Chin. Sci. Bull. 58, 4647–4654.

Li, X.K., Chen, J., Wang, R.C., Li, C., 2018. Temporal and spatial variations of late Mesozoic granitoids in the SW Qiangtang, Tibet: Implications for crustal architecture, Meso-Tethyan evolution and regional mineralization. Earth Sci. Rev. 185, 374–396.

Liu, D.L., Shi, R.D., Ding, L., Huang, Q.S., Zhang, X.R., Yue, Y.H., Zhang, L.Y., 2017. Zircon U–Pb age and Hf isotopic compositions of Mesozoic granitoids in southern Qiangtang, Tibet: implications for the subduction of the Bangong–Nujiang Tethyan Ocean. Gondw. Res. 41, 157–172.

Liu, T., Zhai, Q.G., Wang, J., Bao, P.S., Qiangba, Z., Tang, S.H., Tang, Y., 2016. Tectonic significance of the Dongqiao ophiolite in the north-central Tibetan plateau: evidence from zircon dating, petrological, geochemical and Sr–Nd–Hf isotopic characterization. J. Asian Earth Sci. 116, 139–154.

Ludwig, K.R., 2003. ISOPLOT 3.00: A Geochronological Toolkit for Microsoft Excel. Berkeley Geochronology Center, California, Berkeley.

Ma, A., Hu, X., Garzanti, E., Han, Z., Lai, W., 2017. Sedimentary and tectonic evolution of the southern Qiangtang basin: Implications for the Lhasa–Qiangtang collision timing. J. Geophys. Res. Solid Earth 122, 4790–4813.

Pan, G.T., Wang, L.Q., Li, R.S., Yuan, S.H., Ji, W.H., Yin, F.G., Zhang, W.P., Wang, B.D., 2012. Tectonic evolution of the Qinghai–Tibet Plateau. J. Asian Earth Sci. 53, 3–14.

Patiño Douce, A.E., Johnston, A.D., 1991. Phase equilibria and melt productivity in the pelitic system: implications for the origin of peraluminous granitoids and aluminous granulites. Contrib. Mineral. Petrol. 107, 202–218.

Peters, S.T., Troll, V.R., Weis, F.A., Dallai, L., Chadwick, J.P., Schulz, B., 2017. Amphibole megacrysts as a probe into the deep plumbing system of Merapi volcano, Central Java, Indonesia. Contrib. Mineral. Petrol. 172, 16.

Pichavant, M., Macdonald, R., 2007. Crystallization of primitive basaltic magmas at crustal pressures and genesis of the calc-alkaline igneous suite: experimental evidence from St Vincent, lesser Antilles arc. Contrib. Mineral. Petrol. 154, 535–558.

Plank, T., 2005. Constraints from Thorium/Lanthanumon sediment recycling at subduction zones and the evolution of the continents. J. Petrol. 46, 921–944.

Plank, T., Langmuir, C.H., 1998. The chemical composition of subducting sediment and its consequences for the crust and mantle. Chem. Geol. 145, 325–394.

Rapp, R.P., Watson, E.B., 1995. Dehydration melting of metabasalt at 8–32 kbar: Implications for continental growth and crust–mantle recycling. J. Petrol. 36, 891–931.

Raterman, N.S., Robinson, A.C., Cowgill, E.S., 2014. Structure and detrital zircon geochronology of the Domar fold–thrust belt: evidence of pre-Cenozoic crustal thickening of the western Tibetan Plateau. Geol. Soc. Am. Spec. Paper 507, 89–114.

Reubi, O., Blundy, J., 2009. A dearth of intermediate melts at subduction zone volcanoes and the petrogenesis of arc andesites. Nature 461, 1269–1274.

Ridolfi, F., Renzulli, A., Puerini, M., 2010. Stability and chemical equilibrium of amphibole in calc-alkaline magmas: an overview, new thermobarometric formulations and application to subduction-related volcanoes. Contrib. Mineral. Petrol. 160, 45–66.

Rocchi, S., Di Vincenzo, G., Dini, A., Petrelli, M., Vezzoni, S., 2015. Time-space focused intrusion of genetically unrelated arc magmas in the early paleozoic ross-delamerian orogen (morozumi range, Antarctica). Lithos 232, 84–99.

Rogers, G., Macdonald, R., Fitton, J.G., George, R., Smith, M., Barreiro, B., 2000. Two mantle plumes beneath the East African rift system: Sr, Nd, and Pb isotope evidence from Kenya Rift basalts. Earth Planet. Sci. Lett. 176, 387–400.

Rudnick, R.L., Fountain, D.M., 1995. Nature and composition of the continental crust: a lower crustal perspective. Rev. Geophys. 33, 267–309.

Rudnick, R.L., Gao, S., 2003. Composition of the continental crust. Treat. Geochem. 3, 659.

Rutherford, M.J., Devine, J.D., 2003. Magmatic conditions and magma ascent as indicated by hornblende phase equilibria and reactions in the 1995–2002 Soufriere Hills magma. J. Petrol. 44, 1433–1454.

Schmidt, M.W., Poli, S., 2014. Devolatilization during subduction. In: Holland, H.D., Turekian, K.K. (Eds.), The Crust, Treatise on Geochemistry, 2nd ed. Elsevier-Pergamon, Oxford, pp. 669–701.

Sharma, M., 1997. Siberian traps. In: Mahoney, J.J., Coffin, M.F. (Eds.), Large Igneous Provinces: Continental, Oceanic, and Planetary Flood Volcanism. American Geophysical Union, pp. 273–295.

Shellnutt, J.G., Zellmer, G.F., 2010. High-Mg andesite genesis by upper crystal differentiation. J. Geol. Soc. Lond. 167, 1081–1088.

Shimizu, K., Liang, Y., Sun, C., Jackson, C.R., Saal, A.E., 2017. Parameterized lattice strain models for REE partitioning between amphibole and silicate melt. Am. Mineral. 102, 2254–2267.

Shimoda, G., Tatsumi, Y., Nohda, S., Ishizaka, K., Jahn, B.M., 1998. Setouchi high-Mg andesites revisited: geochemical evidence for melting of subducting sediments. Earth Planet. Sci. Lett. 160, 479–492.

Sláma, J., Košler, J., Condon, D.J., Crowley, J.L., Gerdes, A., Hanchar, J.M., Horstwood, M.S.A., Morris, G.A., Nasdala, L., Norberg, N., Schaltegger, U., Schoene, B., Tubrett, M.N., Whitehouse, M.J., 2008. Plešovice zircon—a new natural reference material for U–Pb and Hf isotopic microanalysis. Chem. Geol. 249, 1–35.

Stevenson, R., Henry, P., Gariépy, C., 1999. Assimilation–fractional crystallization origin of Archean Sanukitoid Suites: western Superior Province, Canada. Precambrian Res. 96, 83–99.

Streck, M.J., Leeman, W.P., Chesley, J., 2007. High-magnesian andesite from Mount Shasta: a product of magma mixing and contamination, not a primitive mantle melt. Geology 35, 351–354.

Sui, Q.L., Wang, Q., Zhu, D.C., Zhao, Z.D., Chen, Y., Santosh, M., Hu, Z.C., Yuan, H.L., Mo, X.X., 2013. Compositional diversity of ca. 110 Ma magmatism in the northern Lhasa Terrane, Tibet: implications for the magmatic origin and crustal growth in a continent–continent collision zone. Lithos 168–169, 144–159.

Sun, S.S., McDonough, W.F., 1989. Chemical and isotopic systematics of oceanic basalts: implications for mantle composition and processes. Geol. Soc. Lond. Spec. Publ. 42, 313–345.

Tang, Y., Zhai, Q.G., Hu, P.Y., Xiao, X.C., Wang, H.T., Wang, W., Zhu, Z.C., Wu, H., 2019. Jurassic high-Mg andesitic rocks in the middle part of the Bangong-Nujiang suture zone, Tibet: New constraints for the tectonic evolution of the Meso-Tethys Ocean. Acta Petrol. Sin. 35, 3097–3114.

Tatsumi, Y., Hanyu, T., 2003. Geochemical modeling of dehydration and partial melting of subducting lithosphere: toward a comprehensive understanding of high-Mg andesite formation in the Setouchi volcanic belt, SW Japan. Geochem. Geophys. Geosyst. 4.

Turner, S., Handler, M., Bindeman, I., Suzuki, K., 2009. New insights into the origin of O–Hf–Os isotope signatures in arc lavas from Tonga–Kermadec. Chem. Geol. 266, 187–193.

Valley, J.W., Kinny, P.D., Schulze, D.J., Spicuzza, M.J., 1998. Zircon megacrysts from kimberlite: oxygen isotope variability among mantle melts. Contrib. Mineral. Petrol. 133, 1–11.

Valley, J.W., Lackey, J.S., Cavosie, A.J., Clechenko, C.C., Spicuzza, M.J., Basei, M.A.S., Bindeman, I.N., Ferreira, V.P., Sial, A.N., King, E.M., 2005. 4.4 billion years of crustal maturation: oxygen isotope ratios of magmatic zircon. Contrib. Mineral. Petrol. 150, 561–580.

Wang, B.D., Wang, L.Q., Chung, S.L., Chen, J.L., Yin, F.G., Liu, H., Li, X.B., Chen, L.K., 2016. Evolution of the Bangong–Nujiang Tethyan Ocean: Insights from the geochronology and geochemistry of mafic rocks within ophiolites. Lithos 245, 18–33.

Wang, L.Q., Pan, G.T., Ding, J., Yao, D.S., 2013. Guidebook of 1:1,500,000 Geological Map of the Qinghai–Xizang (Tibet) Plateau and Adjacent Areas. Geological Publishing House, Beijing, China, pp. 1–288.

Wang, Q., Wyman, D.A., Xu, J.F., Wan, Y.S., Li, C.F., Zi, F., Jiang, Z.Q., Qiu, H.N., Chu, Z.Y., Zhao, Z.H., 2008. Triassic Nb-enriched basalts, magnesian andesites, and adakites of the Qiangtang terrane (Central Tibet): evidence for metasomatism by slab-derived melts in the mantle wedge. Contrib. Mineral. Petrol. 155, 473–490.

Wang, Q., Li, Z.X., Chung, S.L., Wyman, D.A., Sun, Y.L., Zhao, Z.H., Zhu, Y.T., Qiu, H.N., 2011. Late Triassic high-Mg andesite/dacite suites from northern Hohxil, North Tibet: geochronology, geochemical characteristics, petrogenetic processes and tectonic implications. Lithos 126, 54–67.

Wilson, M., 1989. Igneous Petrogenesis. Springer, Harper Collins Academic, London, p. 466.

Woodhead, J.D., Hergt, J.M., Davidson, J.P., Eggins, S.M., 2001. Hafnium isotope evidence for 'conservative' element mobility during subduction zone processes. Earth Planet. Sci. Lett. 192, 331–346.

Xie, L.W., Zhang, Y.B., Zhang, H.H., Sun, J.F., Wu, F.Y., 2008. In situ simultaneous determination of trace elements, U–Pb and Lu–Hf isotopes in zircon and baddeleyite. Chin. Sci. Bull. 53, 1565–1573.

Xu, W., Li, C., Xu, M.J., Wu, Y.W., Fan, J.J., Wu, H., 2015. Petrology, geochemistry, and geochronology of boninitic dikes from the Kangqiong ophiolite: implications for the early cretaceous evolution of Bangong–Nujiang Neo-Tethys Ocean in Tibet. Int. Geol. Rev. 57, 2028–2043.

Yan, M., Zhang, D., Fang, X., Ren, H., Zhang, W., Zan, J., Song, C., Zhang, T., 2016. Paleomagnetic data bearing on the Mesozoic deformation of the Qiangtang block: implications for the evolution of the Paleo- and Meso-tethys. Gondw. Res. 39, 292–316.

Yin, A., Harrison, T.M., 2000. Geologic evolution of the Himalayan-Tibetan orogen. Annu. Rev. Earth Planet. Sci. 28, 211–280.

Zeng, Y.C., Chen, J.L., Xu, J.F., Wang, B.D., Huang, F., 2016. Sediment melting during subduction initiation: Geochronological and geochemical evidence from the Darutso high-Mg andesites within ophiolite melange, Central Tibet. Geochem. Geophys. Geosyst. 17, 4859–4877.

Zhang, C., Ma, C.Q., Holtz, F., Koepke, J., Wolff, P.E., Berndt, J., 2013. Mineralogical and geochemical constraints on contribution of magma mixing and fractional crystallization

to high-Mg adakite-like diorites in eastern Dabie orogen, East China. Lithos 172–173, 118–138.
Zhang, L., Ren, Z.Y., Xia, X.P., Li, J., Zhang, Z.F., 2015. Isotope maker: a Matlab program for isotopic data reduction. Int. J. Mass Spectr. 392, 118–124.
Zhang, L., Ren, Z.Y., Xia, X.P., Yang, Q., Hong, L.B., Wu, D., 2019. In situ determination of trace elements in melt inclusions using laser ablation-inductively coupled plasma-sector field-mass spectrometry. Rapid Commun. Mass Spectrom. 33, 361–370.
Zhang, X., Shi, R., Huang, Q., Liu, D., Gong, X., Chen, S., Wu, K., Yi, G., Sun, Y., Ding, L., 2014. Early Jurassic high-pressure metamorphism of the Amdo terrane, Tibet: constraints from zircon U-Pb geochronology of mafic granulites. Gondw. Res. 26, 975–985.
Zheng, Y.F., Wu, Y.B., Chen, F.K., Gong, B., Li, L., Zhao, Z.F., 2004. Zircon U-Pb and oxygen isotope evidence for a large-scale ^{18}O depletion event in igneous rocks during the Neoproterozoic. Geochim. Cosmochim. Acta 68, 4145–4165.
Zheng, Y.F., Chen, Y.X., Dai, L.Q., Zhao, Z.F., 2015. Developing plate tectonics theory from oceanic subduction zones to collisional orogens. Sci. China Earth Sci. 585, 1045–1069.
Zhong, Y., Liu, W.L., Xia, B., Liu, J.N., Guan, Y., Yin, Z.X., Huang, Q.T., 2017. Geochemistry and geochronology of the Mesozoic Lanong ophiolitic mélange, northern Tibet: Implications for petrogenesis and tectonic evolution. Lithos 292, 111–131.
Zhu, D.C., Zhao, Z.D., Niu, Y., Mo, X.X., Chung, S.L., Hou, Z.Q., 2011. The Lhasa Terrane: record of a microcontinent and its histories of drift and growth. Earth Planet. Sci. Lett. 301, 241–255.
Zhu, Z., Zhai, Q., Hu, P., Chung, S., Tang, Y., Wang, H., Wu, H., Wang, W., Huang, Z., Lee, H., 2019b. Closure of the Bangong–Nujiang Tethyan Ocean in the Central Tibet: results from the provenance of the Duoni Formation. J. Sediment. Res. 89, 1039–1054.
Zhu, D.C., Zhao, Z.D., Niu, Y.L., Dilek, Y., Hou, Z.Q., Mo, X.X., 2013. The origin and pre-Cenozoic evolution of the Tibetan Plateau. Gondw. Res. 23, 1429–1454.
Zhu, D.C., Li, S.M., Cawood, P.A., Wang, Q., Zhao, Z.D., Liu, S.A., Wang, L.Q., 2016. Assembly of the Lhasa and Qiangtang terranes in Central Tibet by divergent double subduction. Lithos 245, 7–17.
Zhu, R.Z., Lai, S.C., Qin, J.F., Zhao, S.W., Santosh, M., 2019a. Petrogenesis of high-K calc-alkaline granodiorite and its enclaves from the SE Lhasa block, Tibet (SW China): implications for recycled subducted sediments. Geol. Soc. Am. Bull. 131, 1224–1238.
Zhu, R.Z., Lai, S.C., Santosh, M., Qin, J.F., Zhao, S.W., 2017. Early cretaceous Na-rich granitoids and their enclaves in the Tengchong Block, SW China: Magmatism in relation to subduction of the Bangong–Nujiang Tethys Ocean. Lithos 286, 175–190.
Zhu, R.Z., Lai, S.C., Qin, J.F., Zhao, S.W., Santosh, M., 2018. Strongly peraluminous fractionated S-type granites in the Baoshan Block, SW China: implications for two-stage melting of fertile continental materials following the closure of Bangong–Nujiang Tethys. Lithos 178–198.